

**This item is the archived peer-reviewed author-version of:**

Size of cerium dioxide support nanocrystals dictates reactivity of highly dispersed palladium catalysts

**Reference:**

Muravev Valery, Parastaev Alexander, van den Bosch Yannis, Ligt Bianca, Claes Nathalie, Bals Sara, Kosinov Nikolay, Hensen Emiel J.M..- Size of cerium dioxide support nanocrystals dictates reactivity of highly dispersed palladium catalysts  
Science / American Association for the Advancement of Science [Washington, D.C.] - ISSN 0036-8075 - 380:6650(2023), p. 1174-1179  
Full text (Publisher's DOI): <https://doi.org/10.1126/SCIENCE.ADF9082>  
To cite this reference: <https://hdl.handle.net/10067/1971990151162165141>

# Size of ceria support nanocrystals dictates reactivity of highly-dispersed palladium catalysts

Valery Muravev<sup>1</sup>, Alexander Parastaev<sup>1</sup>, Yannis van den Bosch<sup>1</sup>, Bianca Ligt<sup>1</sup>, Nathalie Claes<sup>2</sup>, Sara Bals<sup>2</sup>, Nikolay Kosinov<sup>1</sup>, Emiel J.M. Hensen<sup>1\*</sup>

## Affiliations:

<sup>1</sup>Laboratory of Inorganic Materials and Catalysis, Department of Chemical Engineering and Chemistry, Eindhoven University of Technology; 5600 MB Eindhoven, The Netherlands

<sup>3</sup>EMAT, University of Antwerp, 2020 Antwerp, Belgium

\*Corresponding authors. Email: [e.j.m.hensen@tue.nl](mailto:e.j.m.hensen@tue.nl).

**Abstract:** The catalytic performance of heterogeneous catalysts can be tuned by modulation of the size and structure of supported transition metals, typically regarded as the active sites. In single-atom metal catalysts, the support itself can strongly impact the catalytic properties. Here we demonstrate that the size of ceria (CeO<sub>2</sub>) support governs the reactivity of atomically dispersed palladium in carbon monoxide (CO) oxidation. Catalysts with small ceria nanocrystals (4 nanometers) exhibit unusually high activity in a CO-rich reaction feed, whereas catalysts with medium-size ceria (8 nanometers) are preferred for lean conditions. Detailed spectroscopic investigations reveal support size-dependent redox properties of the palladium-ceria interface.

**One-Sentence Summary:** Control over the size of metal oxide support allows for tuning the activity of noble metal heterogeneous catalysts.

**Main Text:** Development of sustainable and efficient chemical processes heavily relies on catalysts. Most heterogeneous catalysts are based on transition metal nanoparticles (NPs) finely dispersed over an inexpensive solid metal oxide support. The high surface-to-volume ratio of supported NPs increases metal utilization, which is particularly important for structure-insensitive reactions catalyzed by precious noble metals (1). To maximize the use of these highly active, yet costly metals, catalysts with atomically dispersed metals (single-atom catalysts, SACs) are being extensively developed (2–5).

Decreasing the size of noble metal species impacts their reactivity (1, 6–8). For example, size-induced perturbations in the electronic structure of few-nanometer gold clusters on titanium dioxide render them remarkably active in low-temperature carbon monoxide (CO) oxidation, in contrast to larger gold NPs (9–11). However, further dispersing metal entities down to single atoms can also adversely affect catalytic activity. For example, clusters of metallic platinum supported on oxides of silicon and zirconium are more reactive toward CO oxidation than isolated platinum species (12). In SACs, every (noble) metal center is coordinated by the atoms of the support. Hence, the chemical properties of the support and metal-support interactions (MSIs) strongly modulate the activity of the catalyst (13–16).

Cerium dioxide (ceria,  $\text{CeO}_2$ ), a key component of automotive catalytic converters, is particularly known for strong MSIs with noble metals, rendering them stable in highly dispersed form (17–19). To limit agglomeration of the active phase in noble-metal SACs, low metal loadings, high-surface-area (nanosized) supports, or both are commonly used (20–24). Nanostructuring can notably change the chemical properties of ceria (25–28). Combining a surface science approach with theoretical calculations, Vayssilov et al. demonstrated that lattice oxygen atoms can spontaneously migrate from nanosized ceria to platinum clusters (~2 nm), a process that is energetically unfavorable on extended  $\text{CeO}_2$  surfaces (29). Carrettin et al. used small (~4 nm) crystallites instead of bulk  $\text{CeO}_2$  as a support for 3-nm gold NPs to achieve a two orders of magnitude increase in low-temperature CO oxidation activity (30).

The effect of ceria particle size on the catalytic properties of atomically dispersed noble metals, however, is yet unexplored. We used flame spray pyrolysis (31) to prepare in a single step palladium-ceria SACs with variable size of the support (4 to 18 nm). Using CO oxidation as a probe reaction, we demonstrate that the reactivity of the prepared nanocomposites strongly depended on the size of ceria particles. Through a combination of advanced in situ spectroscopy

tools and steady-state kinetic studies, the strong impact of the size-dependent redox properties of the palladium-ceria interface on the catalytic performance is highlighted. This work demonstrates an unconventional approach to tailoring the properties of metal-based catalysts by changing the size of the support.

### Pd catalysts with different sizes of CeO<sub>2</sub> support

To prepare ceria with variable sizes, we used flame spray pyrolysis (FSP) (32). The size and redox properties of the obtained ceria NPs was controlled by the injection rate of the liquid feed containing cerium precursor during FSP (figs. S1 to S4). We prepared 1 wt % Pd/CeO<sub>2</sub> catalysts (PdFSP) in a one-step FSP process using a solution containing both metal precursors, which resulted in partial doping of ceria with the noble metal (31). High-resolution high-angle annular dark-field scanning transmission electron microscopy (HAADF-STEM) images (Fig. 1A and bright-field STEM displayed in fig. S6) demonstrated that octahedral NPs of Pd/CeO<sub>2</sub> were synthesized. The size range from 4 to 18 nm was obtained by changing the injection rate from 1 to 15 ml/min (table S1). Throughout this work, we focus on three principal sizes of PdFSP catalysts: (i) small 4-nm NPs; (ii) medium 8-nm NPs; and (iii) large 13-nm NPs (Fig. 1A).

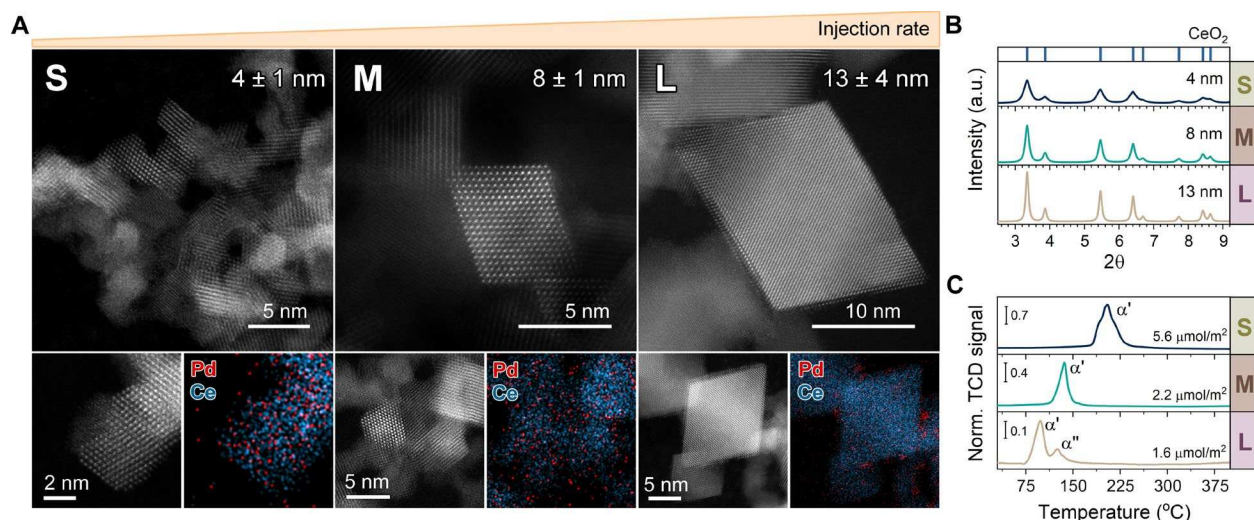


**Fig. 1. Structure and reducibility of FSP-derived 1 wt % Pd/CeO<sub>2</sub> nanocomposites with varying size of the CeO<sub>2</sub> support.** (A) HAADF STEM imaging and EDX elemental mapping of prepared materials. Labels “S”, “M” and “L” refer to catalysts with small (~4 nm), medium (~8 nm) and large (~13 nm) size of CeO<sub>2</sub>, respectively. (B) High-resolution synchrotron-based powder XRD data ( $\lambda=0.18233\text{\AA}$ ). (C) H<sub>2</sub>-TPR profiles and hydrogen consumption quantification data.

Elemental mapping by energy-dispersive x-ray spectroscopy (EDX) revealed the highly dispersed nature of Pd species in small and medium PdFSP, whereas additional Pd clusters of ~2 nm could

be seen on large PdFSP after prolonged electron beam exposure (**figs. S7-S8**). Synchrotron-based powder x-ray diffraction (XRD) exhibited exclusively CeO<sub>2</sub> reflections, indicating the absence of Pd/PdO phases (**Fig. 1B**). The sizes of PdFSP crystallites derived from XRD data (**fig. S9**) were in good agreement with microscopy and physisorption data (**fig. S10 and table S1**).

The palladium-ceria interactions in PdFSP nanocomposites were strongly affected by the size of CeO<sub>2</sub> as probed by temperature-programmed reduction in hydrogen (H<sub>2</sub>-TPR) (**Fig. 1C and fig. S11**). The first peak of reduction ( $\alpha$ ) in small PdFSP that appeared at  $\sim 200$  °C indicated a strong interaction between CeO<sub>2</sub> and Pd that is typical for a highly-dispersed Pd-oxo species (33). As the size of the PdFSP particles increased, this feature shifted to lower temperature and finally split into two peaks ( $\alpha'$  and  $\alpha''$ ), indicating weaker MSIs in these samples. We attributed an additional reduction peak for large PdFSP to the presence of PdO<sub>x</sub> clusters.

Quantification of H<sub>2</sub>-TPR data (**table S2**) revealed that the reducibility of PdFSP nanocomposites strongly depended on their size, even when normalized to the total surface area. From analysis of x-ray photoelectron spectroscopy (XPS) data, we concluded that Pd in small and medium PdFSP samples (**Fig. 2A and fig. S12**) was present as highly dispersed Pd<sup>2+</sup> species strong interacting with CeO<sub>2</sub> (Pd 3d<sub>5/2</sub> binding energy  $\sim 338$  eV) (31, 34). For large PdFSP NPs ( $> 10$  nm), an additional weak component at  $\sim 336$  eV was observed that we attributed to PdO<sub>x</sub> (x < 1) clusters (31, 35).

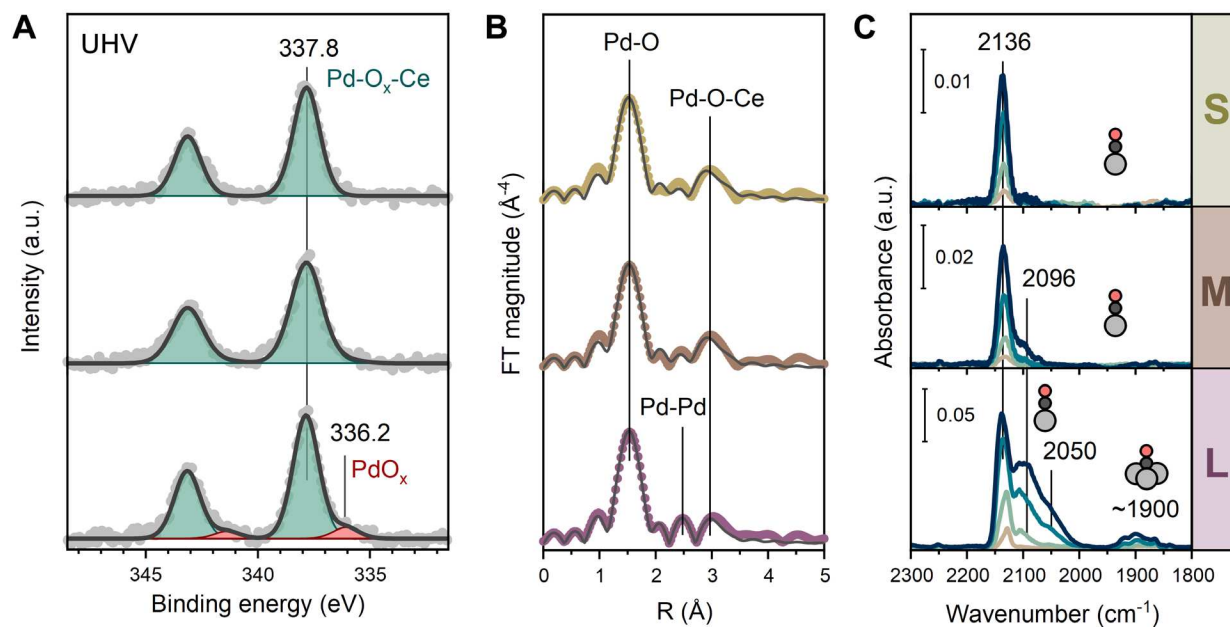


**Fig. 2. Spectroscopic characterization of PdFSP samples with small (S), medium (M), and large (L) CeO<sub>2</sub> NPs. (A)** XPS spectra of Pd 3d core line region acquired for fresh PdFSP samples. **(B)** R-space  $k^3$ -weighted EXAFS spectra of fresh PdFSP samples acquired at the Pd K-edge. **(C)**

In situ DRIFTS during CO adsorption at -20 °C on fresh PdFSP samples. The CO was set to 0.3 ml/min, resulting in a partial pressure of 2 mbar in the DRIFTS cell.

The fitting of Pd K-edge extended x-ray absorption fine structure (EXAFS) revealed the predominantly isolated nature of Pd-oxo species with ~4 oxygen atoms in the first coordination shell and 2 to 3 atoms of Ce in the second shell (**Fig. 2B**, **fig. S13**, and **table S3**) for all samples. However, a weak contribution of Pd-Pd scattering at ~2.7 Å with a coordination number (CN) ~ 1 in the EXAFS of large PdFSP pointed to the presence of small PdO<sub>x</sub> clusters. To probe the speciation of Pd at the very surface of the NPs, we used diffuse reflectance infrared Fourier-transform spectroscopy (DRIFTS) of CO adsorbed at -20 °C (**Fig. 2C**). The in situ DRIFTS spectra of small and medium PdFSP NPs exhibited one major IR band at ~2140 cm<sup>-1</sup> assigned to CO linearly adsorbed on oxidized single-atom Pd species (31, 33, 36, 37). The additional CO bands observed at lower frequencies (2096, 2050 and 1900 cm<sup>-1</sup>) for larger PdFSP NPs could be linked to the presence of semi-reduced and clustered Pd species (31, 33, 36, 37).

Both the overall intensity of carbonyl bands in DRIFTS spectra and the Pd/Ce surface atomic ratios derived from XPS increased with CeO<sub>2</sub> size (**table S1**). These results indicated surface enrichment of Pd on large CeO<sub>2</sub>, which could in turn cause lower Pd dispersion. To test this assumption, we prepared a series of reference Pd/CeO<sub>2</sub> samples using wet impregnation of FSP-made CeO<sub>2</sub> NPs of different sizes (denoted as PdFSPimp, **figs. S14 to S18**, **table S4**). The CO DRIFTS spectra of the low-loaded (0.46 wt%) PdFSPimp sample with large CeO<sub>2</sub> NPs were similar to those of its 1 wt% counterparts prepared by impregnation and the one-step FSP method, displaying bands related to agglomerated Pd species (**fig. S19**).

We inferred that weak MSIs are the most likely reason for the observed clustering of Pd on large CeO<sub>2</sub>. The size of CeO<sub>2</sub> NPs strongly influenced the Pd speciation in both one-step FSP-prepared (PdFSP) and wet-impregnated (PdFSPimp) samples. Strong MSIs in PdFSP NPs of 8 nm and below caused Pd to be exclusively present as isolated sites on and in the CeO<sub>2</sub> surface. Weaker MSIs in large PdFSP NPs (>10 nm) led to coexistence of atomically dispersed and clustered Pd species in the as-prepared catalyst.

### **Pd speciation during catalytic CO oxidation**

We used CO oxidation to probe the activity of FSP-made Pd/CeO<sub>2</sub> nanocomposites. Each catalyst was pretreated in oxygen and subsequently three light-off measurements from -20° to 300°C were performed (**Fig. S20**). All PdFSP catalysts could oxidize CO at room temperature (**Fig. 3A and**

**fig. S21**). Strikingly, the low-temperature CO oxidation activity ( $<100\text{ }^{\circ}\text{C}$ ) strongly depended on the size of the  $\text{CeO}_2$  support. At moderate temperature ( $\sim 150\text{ }^{\circ}\text{C}$ ), small PdFSP displayed a lower activity than medium and large PdFSP, which already achieved full conversion at this temperature. According to light-off catalytic tests, ceria NPs of  $\sim 8\text{ nm}$  were optimal for low-temperature CO oxidation on PdFSP (**Fig. 3B**). Despite the difference in preparation method, the optimal support size for impregnated (PdFSPimp) catalysts was similar (9 nm) and followed the same overall activity trend (**fig. S22**).

We used in situ DRIFTS to shed light on the speciation of Pd under low-temperature CO oxidation conditions ( $75\text{ }^{\circ}\text{C}$ ). **Figure 3(C)** shows that Pd single atoms, represented by the  $\sim 2140\text{ cm}^{-1}$  carbonyl band, remained dominant in small PdFSP, even after reaction at  $300\text{ }^{\circ}\text{C}$ . These sites were particularly active in CO oxidation at low temperature (31, 33, 36, 37). A higher concentration of atomically dispersed Pd in the medium-sized sample, manifested by a more intense  $\sim 2140\text{ cm}^{-1}$  band, could explain its superior activity at low temperatures (**Fig. 3B**).

In contrast to the as-prepared state, low-frequency bands (below  $2100\text{ cm}^{-1}$ ) were also present and likely indicated the formation of metallic Pd clusters during CO oxidation. Metallic Pd species were less active than Pd single atoms at low temperature but could substantially contribute to overall activity  $> 125\text{ }^{\circ}\text{C}$  (31, 38). On large PdFSP, the fraction of metallic and clustered Pd species was considerably higher than that of atomically dispersed Pd, which explained its limited activity at low temperature. The plateauing of the CO oxidation activity at a temperature of  $\sim 125\text{ }^{\circ}\text{C}$  (**Fig. 3A**) on medium and small NPs predominantly populated by isolated Pd species stemmed from the weaker adsorption of CO on single-atom Pd sites as compared to metallic sites (**fig. S23**).

To probe the stability of Pd-oxo species at elevated temperature ( $300\text{ }^{\circ}\text{C}$ ) we used surface-sensitive synchrotron-based near-ambient pressure XPS. During CO oxidation at elevated temperatures, Pd species were stable in the form of highly-dispersed Pd-O<sub>x</sub>-Ce moieties ( $\sim 338\text{ eV}$ ) (**Fig. 3D**). Given that DRIFTS for medium and large PdFSP indicated the formation of reduced Pd clusters at low temperature and even more so after heating up to  $300\text{ }^{\circ}\text{C}$ , we speculate that these clusters were of low nuclearity and may redisperse during CO oxidation at high temperature, akin to the dynamics observed for Pt clusters on  $\text{CeO}_2$  (39). This hypothesis was supported by the minor contribution of Pd-Pd scattering ( $\text{CN}_{\text{Pd-Pd}} \sim 1$ ) in EXAFS of used medium and large PdFSP samples (**fig. S24**). As we noted above, redispersion during CO oxidation at elevated temperature does not occur for larger Pd/PdO NPs on  $\text{CeO}_2$  (38).

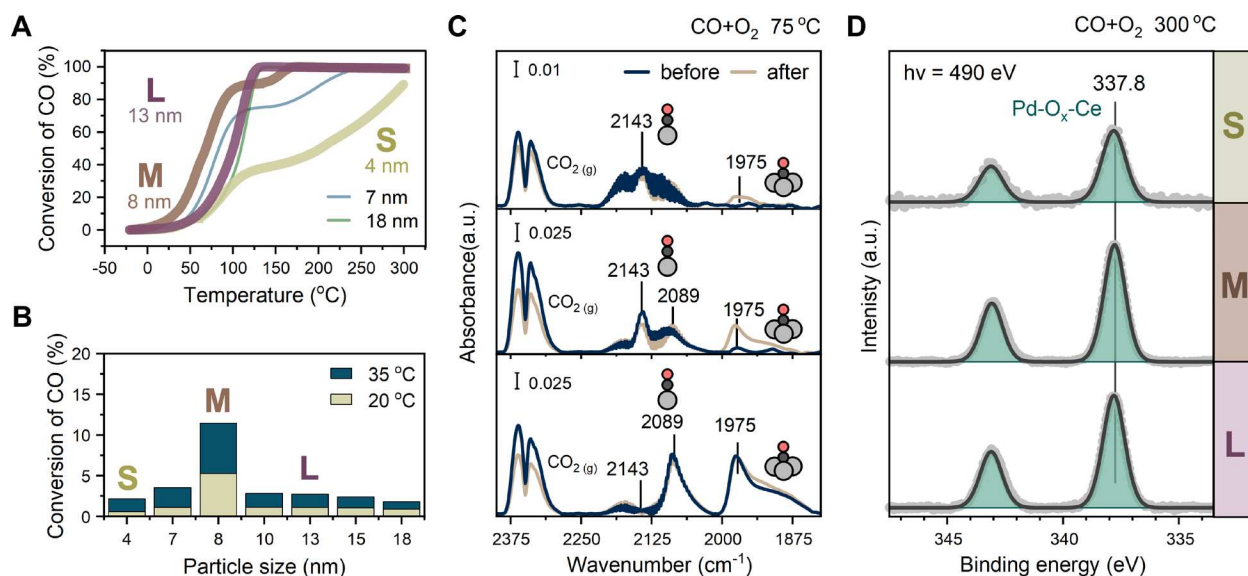


**Fig. 3. Catalytic performance and Pd speciation under reaction conditions.** (A) CO oxidation light-off curves from -20 to 300 °C (3<sup>rd</sup> run). (B) Low-temperature activity as a function of CeO<sub>2</sub> size in PdFSP catalysts. Reaction conditions: 1% CO and 1% O<sub>2</sub> in He (GHSV ~180,000 ml g<sub>cat</sub><sup>-1</sup> h<sup>-1</sup>). (C) In situ DRIFTS spectra acquired during CO oxidation at 75 °C before and after heating up to 300 °C in reaction mixture. Reaction conditions: 1% CO and 1% O<sub>2</sub> in He, total flow 100 ml/min. (D) In situ NAP-XPS Pd 3d spectra of the catalysts exposed to an equimolar CO+O<sub>2</sub> mixture (1 mbar) at 300 °C. Spectra were acquired at 490 eV, corresponding to an inelastic electron mean free path (IMFP) of ca. 5 Å.

The resistance to sintering of single-atom Pd species in small PdFSP NPs originated from the strong MSI. With increasing size of CeO<sub>2</sub>, these interactions became weaker, which resulted in lower stability of atomically dispersed Pd under reaction conditions. The facile transfer of oxygen from the CeO<sub>2</sub> support to Pd sites strongly affected both the activity and stability of Pd-oxo species (31, 33). Hence, it is possible that the observed ceria support size effects stem from the difference in redox properties and oxygen mobility in the prepared nanocomposites.

### Oxygen mobility at palladium-ceria interface

We used in situ resonant photoelectron spectroscopy (RPES) to study the redox properties of palladium-ceria interface in the prepared nanocomposites. This technique allowed us to monitor the Ce<sup>4+</sup>/Ce<sup>3+</sup> ratio at the very surface (inelastic mean free path ~5 Å), minimizing the contribution of bulk Ce atoms (29, 34). As the surface-to-volume ratio changes with the size of PdFSP NPs, RPES is a particularly well-suited spectroscopic probe. The valence band photoelectron spectra of small PdFSP (Fig. 4A) exhibited the highest relative intensity of the Ce<sup>3+</sup> resonant peak (D<sub>Ce<sup>3+</sup></sub>) with respect to the Ce<sup>4+</sup> (D<sub>Ce<sup>4+</sup></sub>) one and off-resonance spectra. As shown in table S5, the fraction of Ce<sup>3+</sup> in CO at 175 °C decreased with the size of ceria NPs, suggesting size-dependent reducibility

of the surface. Interestingly, the reduction of Pd-oxo species was incomplete under these conditions, and medium PdFSP displayed pronounced stabilization of Pd<sup>2+</sup>-O-Ce moieties (**fig. S25**). We infer that oxygen removal by CO involved both Pd and Ce cationic species and was influenced by the size of the support, which was consistent with temperature-programmed reduction in CO (**fig. S26**) and pulsing CO titration (**table S6**) data.

The size-induced changes in redox properties of PdFSP strongly altered the kinetics of CO oxidation. For catalysts with 4 nm ceria, the reaction order in CO was particularly high (+1.3), whereas it decreased drastically for larger NPs (>7 nm) to +0.2 for 13 nm PdFSP (**Fig. 4B**). The opposite trend was observed for the reaction orders in oxygen. For the small PdFSP, it was unusually low (-0.2) and increased to +0.3 for large NPs. The trend in reaction orders was similar for the PdFSP<sub>imp</sub> catalysts (**table S7**). These data suggested that CO oxidation on large PdFSP likely followed the Mars-van Krevelen mechanism, which involves oxygen transfer from the support typical for conventional Pd/CeO<sub>2</sub> catalysts (38).

The unusual reaction orders observed for small PdFSP indicate that oxygen poisoned Pd sites in catalysts with small ceria NPs, necessitating high pressures of CO to achieve high catalytic activity. In a recent theoretical work, such reactivity was ascribed to Pd redox transitions between several formal oxidation states of metal during a catalytic cycle (40). In fact, as shown in **Fig. 4C**, under CO-rich reaction conditions (CO:O<sub>2</sub> = 4:1), small PdFSP exhibited much higher activity than the larger PdFSP NPs. Catalysts highly active under these demanding conditions could contribute to solving the cold-start problem of current emission control systems, where the exhaust feed initially rich in CO limits the activity of conventional noble-metal NP catalysts (41, 42).

To directly probe the evolution of the CO coverage on Pd sites, we performed in situ DRIFTS experiments under conditions similar to those used in the reaction orders study (**Fig. 4D**). A higher partial pressure of CO for large PdFSP caused only minor changes in Pd speciation and the intensity of the CO<sub>2(g)</sub> IR band reflecting the CO oxidation activity. For medium PdFSP, adding more CO increased the activity but also caused reduction and aggregation of Pd-oxo species, as manifested by an increase in the intensity of low-frequency bands (<2100 cm<sup>-1</sup>). In contrast, no additional bands appeared in spectra of small PdFSP exposed to a CO-rich atmosphere. Consistent with the high CO reaction order, the increased CO<sub>2</sub> evolution and intensity of the ~2140 cm<sup>-1</sup> band suggested that CO was competing with O species on single-atom Pd sites during the reaction. We

argue that the high stability of Pd-oxo species in small PdFSP and their poisoning by oxygen arose from facile oxygen transport at the palladium-ceria interface.

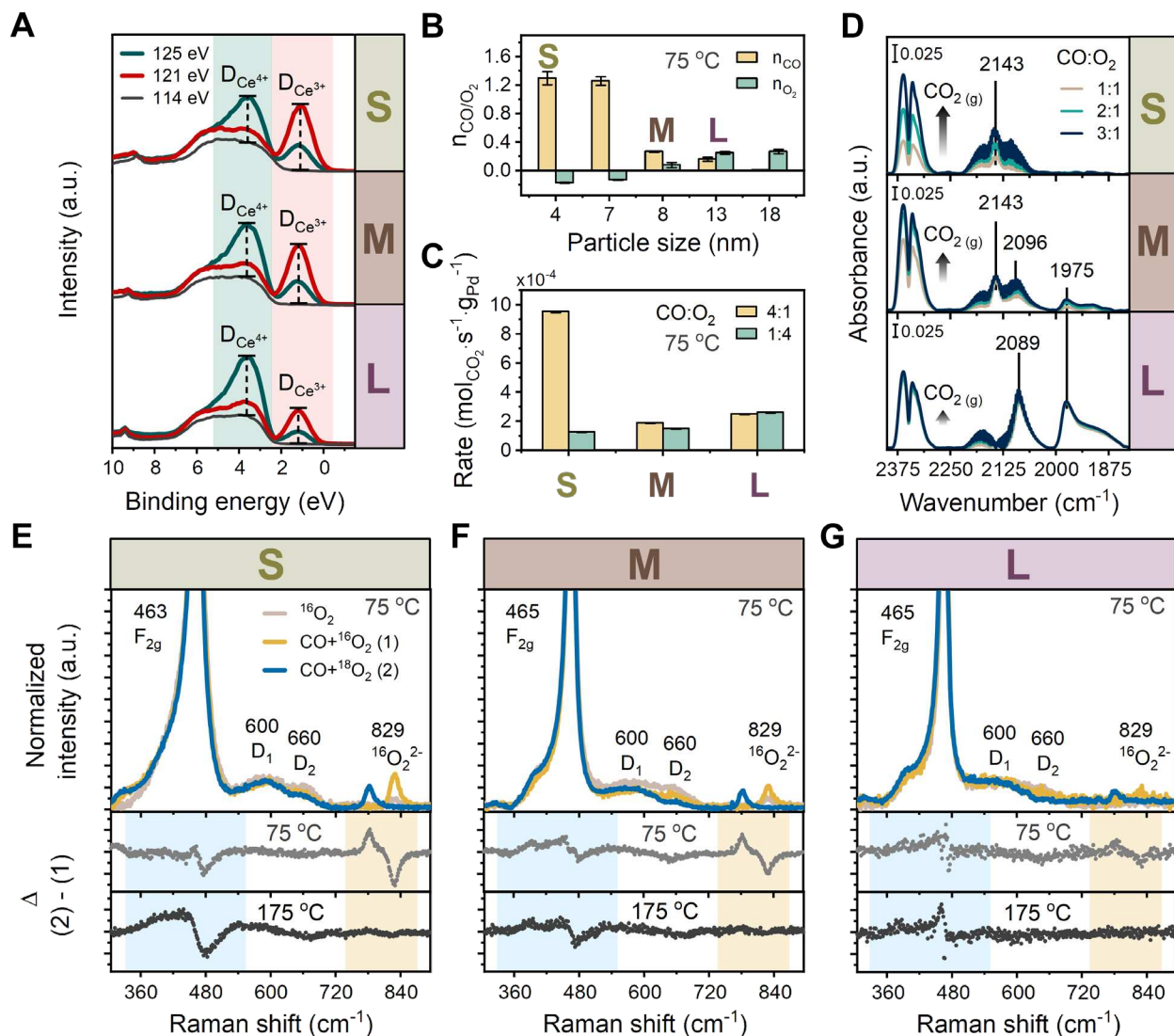


**Fig. 4. CO oxidation kinetics and oxygen transfer at palladium-ceria interface.** (A) In situ RPES valence band spectra of the catalysts exposed to 1 mbar of CO at 175°C. The intensities of the  $\text{Ce}^{4+}$  and  $\text{Ce}^{3+}$  spectral features, which appear at the respective resonant energies (125 eV –  $\text{Ce}^{4+}$ ; 121 eV – for  $\text{Ce}^{3+}$ ; 114 eV – off resonance), were used to estimate the  $\text{Ce}^{3+}$  atomic fraction. (B) Reaction orders measured at 75°C as a function of  $\text{CeO}_2$  size in PdFSP catalysts. Prior to measurements, catalysts were stabilized in the reaction mixture at 75°C for ~14 h. GHSV ~240,000  $\text{ml g}_{\text{cat}}^{-1} \text{h}^{-1}$ , conversion kept below 8%. (C) Steady-state activity at 75 °C in rich ( $\text{CO}:\text{O}_2=4:1$ ) and lean ( $\text{CO}:\text{O}_2=1:4$ ) conditions. GHSV ~240,000  $\text{ml g}_{\text{cat}}^{-1} \text{h}^{-1}$ , conversion kept below 8%. (D) In situ DRIFTS study of CO partial pressure effect on CO oxidation at 75°C on PdFSP samples. Reaction conditions: 1 to 3% of CO and 1% of  $\text{O}_2$  in He at a total flow of 100 ml/min. Prior to changing the partial pressures the catalysts were stabilized on stream for ~30 min. (E to G) Normalized in situ Raman spectra for PdFSP samples in various gas environments. The spectra in isotope-labeled mixture were acquired after 8 h of exposure. Reaction conditions: 1% CO and 1%  $^{16}\text{O}_2$  ( $^{18}\text{O}_2$ ) in He at a total flow of 100 ml/min.

Further evidence for the high oxygen mobility in PdFSP catalysts with small ceria NPs was obtained from in situ Raman spectroscopy coupled with isotope labelling experiments. Following the decreasing size of ceria crystallites in PdFSP, the most intense Ce-O band located at 463 to 465  $\text{cm}^{-1}$  ( $\text{F}_{2\text{g}}$ ) broadened, whereas the relative intensity of bands assigned to intrinsic and extrinsic defects at 600 to 660  $\text{cm}^{-1}$  ( $\text{D}_1$  and  $\text{D}_2$ , see **fig. S27**) increased (**Fig. 4, E to G**) (43, 44). When the  $\text{O}_2$  feed was replaced by a  $\text{CO}+\text{O}_2$  reaction mixture at 75°C, the band at 829  $\text{cm}^{-1}$ , attributed to adsorbed peroxo  $\text{O}_2^{2-}$  species became more intense for all samples, indicated that there was a higher concentration of oxygen vacancies ( $\text{O}_\text{v}$ ) under reaction conditions (33, 43).

In the absence of Pd, the increase in intensity of this peroxo peak was very small upon switching from  $\text{O}_2$  to  $\text{CO}+\text{O}_2$  (**fig. S28**). Accordingly, we conclude that noble metal species induce the formation of  $\text{O}_\text{v}$  and facilitate oxygen activation during low-temperature CO oxidation. The groups of Kwak and Corma arrived at a similar conclusion for Pd/ $\text{CeO}_2$  and Au/ $\text{CeO}_2$  catalysts, respectively (33, 45, 46). To test the possibility of ceria lattice oxygen exchange with gas-phase  $\text{O}_2$  under actual reaction conditions, we replaced the  $\text{C}^{16}\text{O}+^{16}\text{O}_2$  feed by  $\text{C}^{16}\text{O}+^{18}\text{O}_2$  at 75° and 175°C (**Fig. 4, E to G**). As expected from surface adsorbates, the peroxo species exhibited a strong red shift (from 829 to 782  $\text{cm}^{-1}$ ) after complete replacement by  $^{18}\text{O}_2^{2-}$  species (47). After prolonged exposure (8 h), a slight red shift of  $\text{F}_{2\text{g}}$  band was most pronounced for small PdFSP with respect to larger NPs, as evidenced by the difference spectra (**Fig. 4, E to G**, bottom panel). Such a shift indicated partial exchange of  $^{18}\text{O}_2$  with Ce- $^{16}\text{O}$  moieties (48), the extent of which increased at 175°C. Importantly, the shift in  $\text{F}_{2\text{g}}$  band was negligible in Pd-free sample regardless of temperature (**fig. S28**). Altogether in situ Raman data emphasizes the distinctive redox properties of PdFSP catalysts with small  $\text{CeO}_2$  NPs that give rise to facile oxygen transfer at the palladium-ceria interface.

## Discussion

Aimed at maximum utilization of noble metals, the design of highly dispersed catalysts often involves using nanosized metal oxide support materials with a large surface area. We demonstrated that the size of the  $\text{CeO}_2$  support could strongly affect the reactivity of highly dispersed Pd/ $\text{CeO}_2$  catalysts towards oxidation of CO. The observed size dependence was linked to different redox properties of the FSP-prepared Pd/ $\text{CeO}_2$  nanocomposites. The strong MSIs between palladium and ceria and the high oxygen mobility in small PdFSP (4 nm) led to oxygen poisoning of Pd single atoms and limited the activity of the catalyst in low-temperature CO oxidation. Moderate

reducibility of ceria and oxygen mobility at the metal-support interface in medium PdFSP NPs (8 nm) gave rise to a lower reaction order in CO and earlier CO oxidation light-off. Because of weaker MSI and muted oxygen transfer, single Pd atoms are prone to reduction and sintering in large PdFSP (13 nm), which led to inferior activity of the catalyst at low temperature.

We show that by changing the size of ceria support, we could fine-tune the kinetics of low-temperature CO oxidation and achieve high activity, even in CO-rich reaction mixtures. Our results show that high oxygen mobility led to stabilization of atomically dispersed noble metals on small ceria, consistent with the recently reported unusual durability of few-atom Pd, Pt and Rh species on 5-nm CeO<sub>2</sub> supported on alumina (37). The concept of support-size-dependent redox properties of the metal-ceria interface can be extended to other important catalytic reactions involving Ce<sup>3+</sup>/Ce<sup>4+</sup> dynamics, such as CO<sub>2</sub> hydrogenation (49), the water-gas shift reaction (48), and propane dehydrogenation (50).

## References and Notes

1. C. Vogt, B. M. Weckhuysen, The concept of active site in heterogeneous catalysis. *Nat. Rev. Chem.* **6**, 89–111 (2022).
2. A. Wang, J. Li, T. Zhang, Heterogeneous single-atom catalysis. *Nat. Rev. Chem.* **2**, 65–81 (2018).
3. S. K. Kaiser, Z. Chen, D. F. Akl, S. Mitchell, J. Pérez-Ramírez, Single-Atom Catalysts across the Periodic Table. *Chem. Rev.* **120**, 11703–11809 (2020).
4. X. F. Yang, A. Wang, B. Qiao, J. Li, J. Liu, T. Zhang, Single-atom catalysts: A new frontier in heterogeneous catalysis. *Acc. Chem. Res.* **46**, 1740–1748 (2013).
5. L. Liu, A. Corma, Metal Catalysts for Heterogeneous Catalysis: From Single Atoms to Nanoclusters and Nanoparticles. *Chem. Rev.* **118**, 4981–5079 (2018).
6. W. E. Kaden, T. Wu, W. A. Kunkel, S. L. Anderson, Electronic structure controls reactivity of size-selected Pd clusters adsorbed on TiO<sub>2</sub> surfaces. *Science* **326**, 826–829 (2009).
7. J. Li, X. Li, H. J. Zhai, L. S. Wang, Au<sub>20</sub>: A tetrahedral cluster. *Science* **299**, 864–867 (2003).
8. D. A. J. M. Ligthart, R. A. van Santen, E. J. M. Hensen, Supported Rhodium Oxide Nanoparticles as Highly Active CO Oxidation Catalysts. *Angew. Chem. Int. Ed.* **50**, 5306–5310 (2011).
9. M. Valden, X. Lai, D. W. Goodman, Onset of catalytic activity of gold clusters on titania with the appearance of nonmetallic properties. *Science* **281**, 1647–1650 (1998).
10. A. A. Herzing, C. J. Kiely, A. F. Carley, P. Landon, G. J. Hutchings, Identification of active gold nanoclusters on iron oxide supports for CO oxidation. *Science* **321**, 1331–1335 (2008).
11. M. S. Chen, D. W. Goodman, The structure of catalytically active gold on titania. *Science* **306**, 252–255 (2004).
12. K. Ding, A. Gulec, A. M. Johnson, N. M. Schweitzer, G. D. Stucky, L. D. Marks, P. C. Stair, Identification of active sites in CO oxidation and water-gas shift over supported Pt catalysts. *Science* **350**, 189–192 (2015).
13. J. Li, Q. Guan, H. Wu, W. Liu, Y. Lin, Z. Sun, X. Ye, X. Zheng, H. Pan, J. Zhu, S. Chen, W. Zhang, S. Wei, J. Lu, Highly Active and Stable Metal Single-Atom Catalysts Achieved by Strong Electronic Metal–Support Interactions. *J. Am. Chem. Soc.* **141**, 14515–14519 (2019).
14. P. Hu, Z. Huang, Z. Amghouz, M. Makkee, F. Xu, F. Kapteijn, A. Dikhtiarenko, Y. Chen, X. Gu, X. Tang, Catalysis Engineering, Electronic Metal–Support Interactions in Single-Atom Catalysts. *Angew. Chem. Int. Ed.* **53**, 3418–3421 (2014).
15. T. W. van Deelen, C. Hernández Mejía, K. P. de Jong, Control of metal-support interactions in heterogeneous catalysts to enhance activity and selectivity. *Nat. Catal.* **2**, 955–970 (2019).
16. R. Lang, X. Du, Y. Huang, X. Jiang, Q. Zhang, Y. Guo, K. Liu, B. Qiao, A. Wang, T. Zhang, Single-Atom Catalysts Based on the Metal–Oxide Interaction. *Chem. Rev.* **120**, 11986–12043 (2020).
17. A. Beniya, S. Higashi, Towards dense single-atom catalysts for future automotive applications. *Nat. Catal.* **2**, 590–602 (2019).
18. J. A. Farmer, C. T. Campbell, Ceria maintains smaller metal catalyst particles by strong metal-support bonding. *Science* **329**, 933–936 (2010).
19. R. J. Farrauto, M. Deeba, S. Alerasool, Gasoline automobile catalysis and its historical journey to cleaner air. *Nat. Catal.* **2**, 603–613 (2019).
20. L. DeRita, S. Dai, K. Lopez-Zepeda, N. Pham, G. W. Graham, X. Pan, P. Christopher, Catalyst Architecture for Stable Single Atom Dispersion Enables Site-Specific Spectroscopic and Reactivity Measurements of CO Adsorbed to Pt Atoms, Oxidized Pt Clusters, and Metallic Pt Clusters on TiO<sub>2</sub>. *J. Am. Chem. Soc.* **139**, 14150–14165 (2017).
21. J. Resasco, L. Derita, S. Dai, J. P. Chada, M. Xu, X. Yan, J. Finzel, S. Hanukovich, A. S. Hoffman, G. W. Graham, S. R. Bare, X. Pan, P. Christopher, Uniformity Is Key in Defining Structure–Function Relationships for Atomically Dispersed Metal Catalysts: The Case of Pt/CeO<sub>2</sub>. *J. Am. Chem. Soc.* **142**, 169–184 (2020).
22. Y. Lu, J. Wang, L. Yu, L. Kovarik, X. Zhang, A. S. Hoffman, A. Gallo, S. R. Bare, D. Sokaras, T. Kroll, V. Dagle, H. Xin, A. M. Karim, Identification of the active complex for CO oxidation over single-atom Ir-on-MgAl<sub>2</sub>O<sub>4</sub> catalysts. *Nat. Catal.* **2**, 149–156 (2019).
23. J. Fu, J. Lym, W. Zheng, K. Alexopoulos, A. v. Mironenko, N. Li, J. A. Boscoboinik, D. Su, R. T. Weber, D. G. Vlachos, C–O bond activation using ultralow loading of noble metal catalysts on moderately reducible oxides. *Nat. Catal.* **3**, 446–453 (2020).
24. B. Qiao, A. Wang, X. Yang, L. F. Allard, Z. Jiang, Y. Cui, J. Liu, J. Li, T. Zhang, Single-atom catalysis of CO oxidation using Pt<sub>1</sub>/FeOx. *Nat. Chem.* **3**, 634–641 (2011).

25. A. Corma, P. Atienzar, H. García, J.-Y. Chane-Ching, Hierarchically mesostructured doped CeO<sub>2</sub> with potential for solar-cell use. *Nat. Mater.* **3**, 394–397 (2004).
26. D. Prieur, W. Bonani, K. Popa, O. Walter, K. W. Kriegsman, M. H. Engelhard, X. Guo, R. Eloirdi, T. Gouder, A. Beck, T. Vitova, A. C. Scheinost, K. Kvashnina, P. Martin, Size Dependence of Lattice Parameter and Electronic Structure in CeO<sub>2</sub> Nanoparticles. *Inorg. Chem.* **59**, 5760–5767 (2020).
27. C. Paun, O. v. Safonova, J. Szlachetko, P. M. Abdala, M. Nachtegaal, J. Sa, E. Kleymentov, A. Cervellino, F. Krumeich, J. A. van Bokhoven, Polyhedral CeO<sub>2</sub> nanoparticles: Size-dependent geometrical and electronic structure. *J. Phys. Chem. C.* **116**, 7312–7317 (2012).
28. J. Xu, J. Harmer, G. Li, T. Chapman, P. Collier, S. Longworth, S. C. Tsang, Size dependent oxygen buffering capacity of ceria nanocrystals. *Chem. Comm.* **46**, 1887–1889 (2010).
29. G. N. Vayssilov, Y. Lykhach, A. Migani, T. Staudt, G. P. Petrova, N. Tsud, T. Skála, A. Bruix, F. Illas, K. C. Prince, V. Matolín, K. M. Neyman, J. Libuda, Support nanostructure boosts oxygen transfer to catalytically active platinum nanoparticles. *Nat. Mater.* **10**, 310–315 (2011).
30. S. Carrettin, P. Concepción, A. Corma, J. M. López Nieto, V. F. Puentes, Nanocrystalline CeO<sub>2</sub> Increases the Activity of Au for CO Oxidation by Two Orders of Magnitude. *Angew. Chem. Int. Ed.* **43**, 2538–2540 (2004).
31. V. Muravev, G. Spezzati, Y.-Q. Su, A. Parastaev, F.-K. Chiang, A. Longo, C. Escudero, N. Kosinov, E. J. M. Hensen, Interface dynamics of Pd–CeO<sub>2</sub> single-atom catalysts during CO oxidation. *Nat. Catal.* **4**, 469–478 (2021).
32. L. Mädler, W. J. Stark, S. E. Pratsinis, Flame-made ceria nanoparticles. *J. Mater. Res.* **17**, 1356–1362 (2002).
33. Y. Kim, G. Collinge, M. S. Lee, K. Khivantsev, S. J. Cho, V. A. Glezakou, R. Rousseau, J. Szanyi, J. H. Kwak, *Angew. Chem. Int. Ed.*, **60**, 22769–22775.
34. A. Neitzel, A. Figueroba, Y. Lykhach, T. Skala, M. Vorokhta, N. Tsud, S. Mehl, K. Sevcikova, K. C. Prince, K. M. Neyman, V. Matolin, J. Libuda, Atomically Dispersed Pd, Ni, and Pt Species in Ceria-Based Catalysts: Principal Differences in Stability and Reactivity. *J. Phys. Chem. C.* **120**, 9852–9862 (2016).
35. O. A. Stonkus, T. Y. Kardash, E. M. Slavinskaya, V. I. Zaikovskii, A. I. Boronin, Thermally Induced Structural Evolution of Palladium-Ceria Catalysts. Implication for CO Oxidation. *ChemCatChem.* **11**, 3505–3521 (2019).
36. D. Jiang, G. Wan, C. E. García-Vargas, L. Li, X. I. Pereira-Hernández, C. Wang, Y. Wang, Elucidation of the Active Sites in Single-Atom Pd<sub>1</sub>/CeO<sub>2</sub> Catalysts for Low-Temperature CO Oxidation. *ACS Catal.* **10**, 11356–11364 (2020).
37. H. Jeong, O. Kwon, B. S. Kim, J. Bae, S. Shin, H. E. Kim, J. Kim, H. Lee, Highly durable metal ensemble catalysts with full dispersion for automotive applications beyond single-atom catalysts. *Nat. Catal.* **3**, 368–375 (2020).
38. V. Muravev, J. F. M. Simons, A. Parastaev, M. A. Verheijen, J. J. C. Struijs, N. Kosinov, E. J. M. Hensen, Operando Spectroscopy Unveils the Catalytic Role of Different Palladium Oxidation States in CO Oxidation on Pd/CeO<sub>2</sub> Catalysts. *Angew. Chem. Int. Ed.* **61**, e202200434 (2022).
39. F. Maurer, J. Jelic, J. Wang, A. Gänzler, P. Dolcet, C. Wöll, Y. Wang, F. Studt, M. Casapu, J.-D. Grunwaldt, Tracking the formation, fate and consequence for catalytic activity of Pt single sites on CeO<sub>2</sub>. *Nat. Catal.* **3**, 824–833 (2020).
40. L. Wang, S. Deo, A. Mukhopadhyay, I. Nicholas A. Pantelis, M. J. Janik, R. M. Rioux, Emergent Behavior in Oxidation Catalysis over Single-Atom Pd on a Reducible CeO<sub>2</sub> Support via Mixed Redox Cycles. *ACS Catal.* **12**, 12927–12941 (2022).
41. D. S. Lafyatis, G. P. Ansell, S. C. Bennett, J. C. Frost, P. J. Millington, R. R. Rajaram, A. P. Walker, T. H. Ballinger, Ambient temperature light-off for automobile emission control. *Appl. Catal. B.* **18**, 123–135 (1998).
42. D. S. Lafyatis, T. H. Ballinger, G. S. Lammey, J. C. Frosj, B. J. Cooper, The use of catalysts with ambient temperature activity for the control of cold-start automotive emissions. *Stud. Surf. Sci. Catal.* **121**, 383–386 (1999).
43. S. Loidant, Raman spectroscopy as a powerful tool to characterize ceria-based catalysts. *Catal. Today*, **373**, 98–111 (2020).
44. E. Sartoretti, C. Novara, F. Giorgis, M. Piumetti, S. Bensaid, N. Russo, D. Fino, In situ Raman analyses of the soot oxidation reaction over nanostructured ceria-based catalysts. *Sci. Rep.* **9**, 1–14 (2019).
45. J. Guzman, S. Carrettin, J. C. Fierro-Gonzalez, Y. Hao, B. C. Gates, A. Corma, J. Guzman, S. Carrettin, A. Corma, J. C. Fierro-Gonzalez, Y. Hao, B. C. Gates, CO Oxidation Catalyzed by Supported Gold:

- Cooperation between Gold and Nanocrystalline Rare-Earth Supports Forms Reactive Surface Superoxide and Peroxide Species. *Angew. Chem. Int. Ed.* **44**, 4778–4781 (2005).
46. J. Guzman, S. Carrettin, A. Corma, Spectroscopic evidence for the supply of reactive oxygen during CO oxidation catalyzed by gold supported on nanocrystalline CeO<sub>2</sub>. *J. Am. Chem. Soc.* **127**, 3286–3287 (2005).
  47. Z. Wu, M. Li, J. Howe, H. M. Meyer, S. H. Overbury, Probing defect sites on CeO<sub>2</sub> nanocrystals with well-defined surface planes by Raman spectroscopy and O<sub>2</sub> adsorption. *Langmuir*. **26**, 16595–16606 (2010).
  48. C. Schilling, C. Hess, Elucidating the Role of Support Oxygen in the Water-Gas Shift Reaction over Ceria-Supported Gold Catalysts Using Operando Spectroscopy. *ACS Catal.* **9**, 1159–1171 (2019).
  49. A. Parastaev, V. Muravev, E. Huertas Osta, A. J. F. van Hoof, T. F. Kimpel, N. Kosinov, E. J. M. Hensen, Boosting CO<sub>2</sub> hydrogenation via size-dependent metal–support interactions in cobalt/ceria-based catalysts. *Nat. Catal.* **3**, 526–533 (2020).
  50. F. Xing, Y. Nakaya, S. Yasumura, K. Shimizu, S. Furukawa, Ternary platinum–cobalt–indium nanoalloy on ceria as a highly efficient catalyst for the oxidative dehydrogenation of propane using CO<sub>2</sub>. *Nat. Catal.* **5**, 55–65 (2022).
  51. F. Meierhofer, L. Mädler, U. Fritsching, Nanoparticle evolution in flame spray pyrolysis—Process design via experimental and computational analysis. *AIChE J.* **66**, e16885 (2020).
  52. F. Giordano, A. Trovarelli, C. de Leitenburg, M. A. Giona, Model for the Temperature-Programmed Reduction of Low and High Surface Area Ceria. *J. Catal.* **193**, 273–282 (2000).
  53. E. Peterson, A. DeLaRiva, S. Lin, R.S. Johnson, H. Guo, J.T. Miller, J.H. Kwak, C.H.F. Peden, B. Kiefer, L.F. Allard, F.H. Ribeiro, A.K. Datye, Low-temperature carbon monoxide oxidation catalysed by regenerable atomically dispersed palladium on alumina. *Nat. Commun.* **5**, 4885 (2014).
  54. E. Río, S.E. Collins, A. Aguirre, X. Chen, J.J. Delgado, J.J. Calvino, S. Bernal, Reversible deactivation of a Au/Ce<sub>0.62</sub>Zr<sub>0.38</sub>O<sub>2</sub> catalyst in CO oxidation: A systematic study of CO<sub>2</sub>-triggered carbonate inhibition. *J. Catal.* **316**, 210–218 (2014).
  55. S. Zhang, X. Li, B. Chen, X. Zhu, C. Shi, A. Zhu, CO Oxidation Activity at Room Temperature over Au/CeO<sub>2</sub> Catalysts: Disclosure of Induction Period and Humidity Effect, *ACS Catal.* **4**, 3481–3489 (2014)
  56. C. Schilling, C. Hess, CO Oxidation on Ceria Supported Gold Catalysts Studied by Combined Operando Raman/UV–Vis and IR Spectroscopy. *Top. Catal.* **60**, 131–140 (2017).
  57. D. Prieur, W. Bonani, K. Popa, O. Walter, K.W. Kriegsman, M. H. Engelhard, X. Guo, R. Eloiroid, T. Gouder, A. Beck, T. Vitova, A. C. Scheinost, K. Kvashnina, P. Martin, Size Dependence of Lattice Parameter and Electronic Structure in CeO<sub>2</sub> Nanoparticles. *Inorg. Chem.* **59**, 5760–5767 (2020).
  58. K. Priolkar, P. Bera, P.R. Sarode, M.S. Hegde, S. Emura, R. Kumashiro, N.P. Lalla, Formation of Ce<sub>1-x</sub>Pd<sub>x</sub>O<sub>2-δ</sub> Solid Solution in Combustion-Synthesized Pd/CeO<sub>2</sub> Catalyst: XRD, XPS, and EXAFS Investigation. *Chem. Mater.* **14**, 2120–2128 (2002).
  59. H. Liang, J.M. Raitano, G. He, A. Akey, I. Herman, L. Zhang, S. Chan, Aqueous co-precipitation of Pd-doped cerium oxide nanoparticles: chemistry, structure, and particle growth. *J. Mater. Sci.* **47**, 299–307 (2012).
  60. D. Marrocchelli, S.R. Bishop, H.L. Tuller, B. Yildiz, Understanding Chemical Expansion in Non-Stoichiometric Oxides: Ceria and Zirconia Case Studies. *Adv. Funct. Mater.*, **22**: 1958–1965 (2012).
  61. F. Zhang, Z. Liu, S. Zhang, N. Akter, R.M. Palomino, D. Vovchok, I. Orozco, D. Salazar, J.A. Rodriguez, J. Llorca, J. Lee, D.H. Kim, W. Xu, A.I. Frenkel, Y. Li, T. Kim, S.D. Senanayake *ACS Catal.* **8**, 3550–3560 (2018)
  62. M. Kurnatowska, L. Kepinski, W. Mista, Structure evolution of nanocrystalline Ce<sub>1-x</sub>Pd<sub>x</sub>O<sub>2-y</sub> mixed oxide in oxidizing and reducing atmosphere: Reduction-induced activity in low-temperature CO oxidation, *Appl. Cat. B Environ.* **117-118**, 135–147 (2012).
  63. C.I. Hiley, J.M. Fisher, D. Thompsett, R.J. Kashtiban, J. Sloan, R.I. Walton, Incorporation of square-planar Pd<sup>2+</sup> in fluorite CeO<sub>2</sub>: hydrothermal preparation, local structure, redox properties and stability. *J. Mater. Chem. A*, **3**, 13072–13079 (2015).
  64. D.L. Bish and R.C. Reynolds, "4. SAMPLE PREPARATION FOR X-RAY DIFFRACTION" In *Modern Powder Diffraction* edited by David L. Bish and Jeffrey E. Post, 73–100. Berlin, Boston: De Gruyter, 1989.
  65. C. Yang, X. Yu, S. Heißler, A. Nefedov, S. Colussi, J. Llorca, A. Trovarelli, Y. Wang, C. Wöll, Surface Faceting and Reconstruction of Ceria Nanoparticles. *Angew. Chem. Int. Ed.*, **56**, 375 (2017).
  66. A. Chen, X. Yu, Y. Zhou, *et al.* Structure of the catalytically active copper–ceria interfacial perimeter. *Nat Catal.* **2**, 334–341 (2019).
  67. G.N. Vayssilov, M. Mihaylov, P.S. Petkov, K.I. Hadjiivanov, K.M. Neyman, Reassignment of the Vibrational Spectra of Carbonates, Formates, and Related Surface Species on Ceria: A Combined Density Functional and Infrared Spectroscopy Investigation. *J. Phys. Chem. C* **115** (47), 23435–23454 (2011).

68. J.J.C. Struijs, V. Muravev, M.A. Verheijen, E.J.M. Hensen, N. Kosinov, Ceria-Supported Cobalt Catalyst for Low-Temperature Methanation at Low Partial Pressures of CO<sub>2</sub>. *Angew. Chem. Int. Ed.*, **135**, e202214864 (2023).
69. E.M. Köck, M. Kogler, T. Bielz, B. Klötzer, S. Penner, In Situ FT-IR Spectroscopic Study of CO<sub>2</sub> and CO Adsorption on Y<sub>2</sub>O<sub>3</sub>, ZrO<sub>2</sub>, and Ytria-Stabilized ZrO<sub>2</sub>. *J. Phys. Chem. C* **117** (34), 17666-17673, (2013).
70. B. Ravel and M. Newville, *ATHENA, ARTEMIS, HEPHAESTUS*: data analysis for X-ray absorption spectroscopy using *IFEFFIT*. *J. Synchrotron Rad.*, **12**, 537-541, (2005).

**Acknowledgments:** We acknowledge MAX IV Laboratory for time on beamline SPECIES under proposals 20200412 and 20190983. We thank Esko Kokkonen and Alexander Klyushin for assistance with NAP-XPS and RPES experiments conducted at SPECIES. We acknowledge MAX IV Laboratory for time on beamline BALDER under proposal 20200378 and Konstantin Klementiev for assistance with XAS measurements. The synchrotron based XRD measurements were performed on beamline ID31 at the European Synchrotron Radiation Facility (ESRF), Grenoble, France. We are grateful to Jacob Drnec at the ESRF for providing assistance in using beamline ID31. We thank Virginia Perez-Dieste and Ignacio Villar Garcia at CIRCE beamline at ALBA Synchrotron for help with acquiring preliminary RPES data obtained under proposal 2020024219.

**Funding:**

The Netherlands Center for Multiscale Catalytic Energy Conversion (MCEC), a NWO Gravitation program funded by the Ministry of Education, Culture and Science of the government of the Netherlands (VM and EJM).

Research conducted at MAX IV, a Swedish national user facility, is supported by the Swedish Research council under contract 2018-07152, the Swedish Governmental Agency for Innovation Systems under contract 2018-04969, and Formas under contract 2019-02496 (VM).

European Research Council (ERC Consolidator Grant #815128 REALNANO) and European Union's Horizon 2020 research and innovation program under grant agreement No 823717 – ESTEEM (S.B. and N.C)

**Author contributions:**

Conceptualization: VM, EJM

Methodology: VM, AP, NK, SB, EJM

Investigation: VM, AP, YVB, BL, NC, NK

Visualization: VM

Funding acquisition: EJM

Project administration: EJM

Supervision: VM, EJM

Writing – original draft: VM

Writing – review & editing: VM, NK, EJM

**Competing interests:** Authors declare that they have no competing interests.

**Data and materials availability:** All data are available in the main text or the supplementary materials.

## **Supplementary Materials**

Materials and Methods

Supplementary Text

Figs. S1 to S31

Tables S1 to S8

References (51–70)

## Supplementary Materials for

### **Size of ceria support nanocrystals dictates reactivity of highly-dispersed palladium catalysts**

Valery Muravev<sup>1</sup>, Alexander Parastaev<sup>1</sup>, Yannis van den Bosch<sup>1</sup>, Bianca Ligt<sup>1</sup>, Nathalie Claes<sup>2</sup>, Sara Bals<sup>2</sup>, Nikolay Kosinov<sup>1</sup>, Emiel J.M. Hensen<sup>1</sup>

<sup>1</sup>Laboratory of Inorganic Materials and Catalysis, Department of Chemical Engineering and Chemistry, Eindhoven University of Technology; 5600 MB Eindhoven, The Netherlands

<sup>2</sup>EMAT, University of Antwerp, 2020 Antwerp, Belgium

Correspondence to: [e.j.m.hensen@tue.nl](mailto:e.j.m.hensen@tue.nl)

#### **This PDF file includes:**

Materials and Methods  
Supplementary Text  
Figs. S1 to S31  
Tables S1 to S8  
References (51–70)

## Materials and Methods

### Catalyst preparation

FSP synthesis was performed with a TETHIS NPS10 apparatus. Cerium (III) acetate hydrate was dissolved in a mixture (50:50 vol%) of glacial acetic acid and 2-ethylhexanoic acid to yield a 0.15 M precursor solution for CeO<sub>2</sub> synthesis. To ensure complete solubility of cerium acetate, the mixture was mildly heated to 60–70 °C and stirred for 1 h. After cooling to ambient temperature, the solution was used to fill the syringe of the FSP apparatus. To sustain the flame, flows of 1.5 l/min of methane and 3.0 l/min of oxygen were used. Oxygen also served as a dispersion gas at a rate of 5 l/min. The PdFSP samples (1 wt% Pd/CeO<sub>2</sub>) were prepared by one-step FSP. For that an appropriate amount of Pd (II) acetylacetonate was dissolved together with cerium (III) acetate hydrate in a mixture (50:50 vol%) of glacial acetic acid and 2-ethylhexanoic acid to yield 0.15M (based on Ce content) precursor solution. To obtain PdFSP with different particle sizes of the support, the liquid feed injection rate was varied (*i.e.*, 1, 2.5, 5, 7.5, 10, 12.5, and 15 ml/min). At each injection rate, the overpressure at the nozzle was adjusted to 2.5 bar. PdFSPimp catalysts were obtained by wet impregnation of FSP-made CeO<sub>2</sub> supports with 1 wt% Pd (unless stated otherwise). For this purpose, an appropriate amount of Pd(NO<sub>3</sub>)<sub>2</sub>·2H<sub>2</sub>O was dissolved in demineralized water (~10 mL) and the resulting solution was poured onto the CeO<sub>2</sub> powder prepared by FSP at different injection rates (*i.e.*, 1, 2.5, 5, 7.5, 10, 12.5, and 15 ml/min). The suspension was stirred and slowly heated without boiling until it dried. To remove the remaining water the sample was placed in a drying oven overnight. The final step was calcination of the sample at 300 °C in air.

### Catalytic activity measurements

For the catalytic tests, the samples were pressed, crushed, and sieved to a fraction between 125 and 250 µm. The sieved fraction (typically 50 mg) was then mixed with silicon carbide (200–300 mg) to avoid bypassing of the gas flow and formation of hot spots. This mixture was loaded in a quartz tube reactor and enclosed between two quartz wool plugs. The catalysts were pretreated in situ under a flow of 20 vol% O<sub>2</sub> in He at 300 °C for 1 h and then cooled to room temperature. The reactor was flushed with He and cooled to -20 °C by a home-made liquid nitrogen cooling system. The light-off CO oxidation catalytic tests followed by mass-spectrometry were performed from -20 °C to 300 °C at a ramp rate of 5 °C/min. The reaction mixture contained 1 vol% CO and 1 vol% O<sub>2</sub> in He, with a total flow of 150 ml/min. Repeated light-off cycles were performed on the same catalysts after cooling to -20 °C. CO conversion was estimated from the mass-spectrometry (Balzers TPG-300) data by following the CO ( $m/z=28$ ), O<sub>2</sub> ( $m/z=32$ ) and CO<sub>2</sub> ( $m/z=44$ ) signals ( $m/z=44$ ) and was verified by gas chromatography (GC). The GC analysis (Interscience Compact GC 4.0) of effluent was done using RT-Q-Plot and Molsieve columns and thermal conductivity detectors (TCDs). To determine the reaction orders, an appropriate amount of catalyst was loaded to maintain the CO conversion below 8%. The reference reaction mixture was 1 vol% O<sub>2</sub>, 1 vol% CO in He at a total flow of 200 ml/min. Prior to changing the partial pressures of reactants (CO and O<sub>2</sub>), the catalyst was stabilized in the reference reaction feed for ~14 h to reach the steady state. To determine the reaction orders, partial pressures of CO and O<sub>2</sub> were varied from 0.5 vol% to 4 vol%.

### Characterization

Lab-based powder X-ray diffraction measurements were performed on a Bruker Phaser D2 diffractometer with Cu K $\alpha$  source. The crystallite size of PdFSP and PdFSPimp samples was

estimated with the DiffracEva software and the implemented Scherrer equation applied to the CeO<sub>2</sub> reflection at 47.5° corresponding to the (220) crystal plane. Synchrotron-based powder X-ray diffraction was performed at ID31beamline (ESRF, Grenoble) at  $\lambda = 0.18233$  Å. A Dectris Pilatus3X CdTe 2M detector was employed to acquire the data in Debye-Scherrer geometry. Using the GSAS II software, Rietveld refinement was employed to determine the crystallite size of FSP-made CeO<sub>2</sub> nanoparticles.

The N<sub>2</sub> physisorption at -196 °C was performed with TriStar II 3020 apparatus. The Brunauer-Emmet-Teller (BET) method was employed to estimate the surface area of the prepared materials. The size of the nanoparticles was estimated using equation (1) assuming spherical nanoparticles and equation (2) assuming octahedral nanoparticles.  $A_s$  is the surface area determined by BET and  $\rho_p$  is the density of the material (7.2 g/cm<sup>3</sup>). Better correlation with TEM and XRD data was found under assumption of octahedral shape of nanoparticles.

$$d_{BET} (nm) = \frac{6000}{A_s * \rho_p} \quad (1) \qquad d_{BET (octa)}(nm) = \frac{60000}{4 * A_s * \rho_p * \sqrt{2}} \quad (2)$$

ICP-OES was performed to determine the loading of Pd. The measurements were done on an AMETEK SpectroBlue apparatus. Around 25 mg of the sample was dissolved in 5 ml of concentrated H<sub>2</sub>SO<sub>4</sub> at 200 °C. After cooling the solution, demineralized water was added for dilution. All solutions were prepared in duplo to verify the reproducibility of the results. A calibration line with concentrations between 0 and 2 mg/l of Pd was used.

High resolution scanning transmission electron microscopy (HRSTEM) and high-angular images were acquired with an aberration-corrected Thermo Fisher Scientific Titan microscope operated at 120 kV. The sample was deposited on a graphene grid in order to improve the contrast and the stability of the particles. A “beam shower” of 20 minutes was applied before STEM imaging to avoid the build-up of carbon contamination. Energy dispersive X-ray spectroscopy (EDX) measurements were carried out using a ChemiSTEM system and analyzed using the Velox software. The EDX-STEM datasets were acquired with a 150 pA beam current and a total time acquisition of approximately 10 min. An average filter with kernel size 3 was applied to the elemental maps. Bright-field STEM images were collected on a FEI Tecnai 20 microscope operating at acceleration voltage of 200 kV. No less than 100 particles were counted to estimate the average particle size from TEM data.

H<sub>2</sub> temperature-programmed reduction (H<sub>2</sub>-TPR) was performed on a Micromeritics Autochem II 2920. The device was equipped with a U-shaped quartz reactor, a computer-programmed oven, and a thermal conductivity detector (TCD). Around 50–75 mg of catalyst was placed between two quartz wool plugs in the U-shaped reactor. Before the reduction each sample was pretreated in situ to remove adsorbed gasses and impurities. During the pretreatment the sample was heated to 300 °C in a 5 vol% O<sub>2</sub>/He flow at 50 ml/min. After that the sample was cooled down to room temperature and flushed with a flow of helium for 30 min. The reduction was performed using a 4 vol% H<sub>2</sub>/He flow at 50 ml/min and ramping the temperature to 700 °C at a rate of 10 °C/min. The H<sub>2</sub> consumption registered by TCD was then plotted as H<sub>2</sub>-TPR profile.

CO temperature-programmed reduction (CO-TPR) was performed using a home-built setup equipped with an online mass spectrometer (Balzers TPG-300). Typically, around 50 mg of the catalyst was placed in a quartz tube and fixed between plugs of glass wool. All samples were pretreated in situ using a 20 vol% O<sub>2</sub>/He flow at 100 ml/min at 300 °C for 1h. After cooling of the sample to room temperature, the oxygen was turned off and for 20 minutes the reactor was flushed with He. The sample was then cooled to -20 °C by a home-built liquid nitrogen cooling system. Then the flow was switched to 1.33 vol% CO/He with a total flow of 150 ml/min and the reduction

was performed by ramping up the temperature at 10 °C/min from -20 °C to 450 °C. The CO<sub>2</sub> MS signal ( $m/z=44$ ) was used to plot the CO-TPR profiles.

CO pulsing experiments were performed using a home-build pulse setup equipped with a mass spectrometer (Balzers TPG-300). Typically, around 50 mg of the sample was fixed between two quartz wool plugs in a stainless-steel reactor tube. Each sample was pretreated in situ to remove adsorbates and impurities. During pretreatment the sample was heated to 300 °C for 1 h under a 33 vol% O<sub>2</sub>/He flow at 60 ml/min. After that, the sample was cooled in pretreatment flow to 175 °C, followed by switching the flow to pure He and the catalyst was flushed for 1 h at 100 mL/min. After flushing, the flow of He was decreased to 25 ml/min and pulses of CO were introduced every 5 min by a 6-way valve with a sample loop of 100 µL. The amount of CO consumed by the sample was calculated from the peak areas of CO signal ( $m/z=28$ ) and considering fragmentation of CO<sub>2</sub>. CO pulsing was performed until no changes of the peak areas were registered.

Ultrahigh vacuum X-ray photoelectron spectroscopy (XPS) was performed using a Thermo Scientific K-Alpha spectrometer equipped with monochromatized Al K $\alpha$  X-ray source operating at 72 W. Powder samples were deposited on a double-sided carbon tape and the spectra were measured at a pass energy of 50 eV. The dual-beam flood-gun was used to compensate the surface charging. All the spectra were processed using the CasaXPS software package. The binding energy scale was adjusted by the U'''' component of the Ce 3d core line located at 916.7 eV as an internal energy reference (31,35,38,49). The Pd to Ce surface atomic ratios were estimated using respective atomic sensitivity factors. The XPS spectra were fitted using symmetric pseudo-Voigt function, referred to as GL (30) in CasaXPS software. For the Pd 3d spectra containing metallic component, an asymmetric pseudo-Voigt function referred to as LF (0.76, 1.5, 55, 300) in CasaXPS was used. The Ce 3d spectra were fitted according to the models reported earlier (31,49).

Surface-sensitive in situ resonant photoelectron spectroscopy (RPES) and near-ambient pressure X-ray photoelectron spectroscopy (NAP-XPS) were performed at the APXPS endstation of SPECIES beamline at the MAX IV Laboratory. Photoelectron spectra were acquired using a SPECS Phoibos NAP-150 electron analyser featuring a differential pumping system that allowed in situ XPS measurements in a gaseous environment. The experimental geometry implied a normal take-off angle. The analysis chamber was pressurized using calibrated mass flow controllers and high-purity gases. To avoid charging effects, the samples were pressed into aluminium foil and fixed onto the stainless-steel sample holder. For the experiments shown in Fig. 3 (D) and Fig. S25, a pretreatment was performed by heating the samples to 300 °C in 1 mbar of O<sub>2</sub>. The samples were then cooled to ambient temperature and a mixture of CO+O<sub>2</sub> (1:1) was introduced in the analysis chamber and the pressure was fixed to ~1 mbar. Subsequently, the samples were heated to 300 °C in the reaction mixture and stabilized for 30 minutes prior to spectra collection. The Pd 3d core-line spectra were recorded at 490 eV of incident photon energy and 50 eV of pass energy. After a linear background subtraction, the spectral lines were fitted in a similar manner to the lab-based UHV XPS data. For the experiments shown in Fig. 4(A), the catalysts were pretreated in 1 mbar of O<sub>2</sub> at 300 °C, cooled to 75 °C and NAP cell was filled with pure CO (1 mbar). Next, the samples were heated to 175 °C and after stabilization for 30 min, the Pd 3d spectra were acquired at 490 eV of incident photon energy and 50 eV of pass energy. For the RPES study, a variable photon energy was used for selective excitation of Ce 4d–4f transitions related to Ce<sup>3+</sup> and Ce<sup>4+</sup> states (29,31,34). The Ce<sup>3+</sup>/Ce<sup>4+</sup> ratios were determined by the heights of the respective resonant peaks (29,31,34). Following this approach, the concentration of Ce<sup>3+</sup> at the very surface (<1 nm) can be obtained.

Diffuse reflectance infrared Fourier transform spectroscopy (DRIFTS) was carried out using Bruker Vertex 70V with an MCT-detector and Harrick-design in-situ DRIFTS cell. Typically, 25-50 mg of the sample powder was placed in the in situ cell. The thermocouple was in direct contact with the catalyst bed and the temperature was controlled by a PID thermocontroller (Harrick). The sample was pretreated in situ in 20 vol% O<sub>2</sub>/He flow at 300 °C. After cooling to room temperature, the sample was evacuated and further cooled to -20 °C by liquid nitrogen. When the sample was stabilized at -20 °C, a background spectrum was collected. Then CO was admitted at 0.28 ml/min and a total pressure in the cell reached 2 mbar. Upon exposure of the sample to CO, a series of spectra, 50 scans per spectrum in the 3800 - 1000 cm<sup>-1</sup> range and 2 cm<sup>-1</sup> resolution, were acquired until no changes between the collected spectra were visible. For the in situ DRIFTS experiments, the fresh sample was pretreated as described above. After cooling down to 75 °C the background spectrum was acquired, and the flow was switched from 1 vol% O<sub>2</sub> in He (total flow 100 ml/min) to reaction mixture of 1 vol% CO + 1 vol% O<sub>2</sub> in He (total flow 100 ml/min). The catalyst was stabilized for ~30-40 minutes and then an in situ IR spectrum (150 scans) was measured. Then DRIFTS spectra at different stoichiometries of reaction mixture were acquired (1:1, 2:1 and 3:1, of CO to O<sub>2</sub> respectively).

Transmission infrared Fourier-transform spectroscopy study of low-temperature CO adsorption on the bare CeO<sub>2</sub> supports was performed using a Bruker Vertex 70v spectrometer equipped with a DTGS-detector. Approximately 10-15 mg of CeO<sub>2</sub> powder were pressed into self-supporting discs of 13 mm and mounted onto a homebuilt transmission infrared cell. The samples were pretreated at 300 °C in 200 mbar O<sub>2</sub>, cooled to room temperature and evacuated. Subsequently, the sample holder was cooled to -170 °C by supplying liquid N<sub>2</sub> to internal cooling circuit and the background spectra were recorded. After that, 1 mbar of CO was dosed to the cell and the spectra were recorded. Each spectrum was collected by averaging 64 scans with a resolution of 2 cm<sup>-1</sup> in the 4000–1000 cm<sup>-1</sup> range.

X-ray absorption spectroscopy was performed at the BALDER beamline of the MAX IV laboratory in Lund, Sweden. Data were collected at the Pd K edge (24350 eV) in transmission mode. The Pd foil measured in transmission mode was used for energy referencing. The samples were pelletized into self-supporting discs. The collected spectra were background subtracted and normalized using the Athena software package. EXAFS fitting of the *k*<sup>3</sup>-weighted data was performed with the Artemis software. Scattering paths were calculated with FEFF6 using the crystal structures of Pd, PdO and DFT-optimized Pd-doped ceria model (31). The amplitude reduction factor *S*<sub>0</sub><sup>2</sup> was determined by fitting the first-shell Pd–Pd scattering paths in R-space EXAFS spectrum of Pd foil with the coordination number fixed to 12.

In situ Raman spectra were acquired with Witec Alpha 300 Raman microscope equipped with 532 nm laser and 50X Zeiss lens objective. The laser power was limited to 2 mW and the grating was set to 1200 g/mm. Single spectrum was recorded for one minute. The Linkam CCR1000 cell was used for in situ measurements. The samples were pelletized and put into the sample cup of the cell. Each sample was pretreated in 20% O<sub>2</sub> in He (100 ml/min total flow) at 300 °C. Raman spectra were recorded at 75 °C in O<sub>2</sub> and subsequently the reaction feed (1% CO and 1% <sup>16</sup>O<sub>2</sub> in He, 100 ml/min total) was introduced by switching a four-way valve. The spectra were collected, and the reaction mixture was replaced by the labelled feed (1% CO and 1% <sup>18</sup>O<sub>2</sub> in He, 100 ml/min total). Samples were exposed to oxygen-labelled reaction mixture for ~8 h after which the unlabelled feed was introduced. Similar experiment was performed at 175 °C. Averaging and linear background subtraction were performed during processing of the Raman data.

## Supplementary Text

### Size-dependent redox properties of FSP prepared CeO<sub>2</sub> nanoparticles

We prepared a set of ceria supports with different particle sizes using flame spray pyrolysis. Madler et al. (32) showed that the ceria particle size can be controlled by changing the injection rate of the liquid feed during FSP synthesis. This was explained by variations in the residence time and size of the precursor droplets sprayed in the flame, which strongly affect the crystallization process (32, 51). Using cerium acetate as a precursor and a mixture of 2-ethylhexanoic and glacial acetic acid (50:50 vol%) as solvent, we prepared CeO<sub>2</sub> samples at injection rates ranging from 1 to 10 ml/min. Transmission electron microscopy images (Fig. S1) and corresponding particle size distribution plots (Fig. S1) revealed that the size of CeO<sub>2</sub> nanoparticles can be tuned in the range of 5 to 13 nm by adjusting the feed injection rate. Synchrotron powder X-ray diffraction (XRD) patterns of the as-prepared samples (Fig. S2a) only exhibit the characteristic reflections of the cubic phase of ceria (*Fm3m*). The systematic broadening of the diffraction peaks upon decreasing the injection feed rate indicates a decrease in the CeO<sub>2</sub> crystallite size.

The redox properties of the obtained supports were studied using temperature-programmed reduction in hydrogen (H<sub>2</sub>-TPR). For all CeO<sub>2</sub> samples, we can distinguish two main reduction features in the H<sub>2</sub> consumption profiles: a low-temperature peak ( $\alpha$ ) at ~300-325 °C and a broad feature ( $\beta$ ) at 400-500 °C (Fig. S2b). As bulk reduction of CeO<sub>2</sub> usually occurs at higher temperature (*i.e.*, ~800 °C), the  $\alpha$  and  $\beta$  features can be related to surface oxygen reduction (52). A prominent  $\beta$  peak in TPR profiles is typical for CeO<sub>2</sub> with a high surface area, *i.e.*, with a crystallite size smaller than 20 nm (28,52). The  $\alpha$  feature becomes stronger with decreasing particle size. The appearance of this feature at substantially lower temperatures than the  $\beta$  one points to a presence of additional type of reactive oxygen species. Thus, the low-temperature  $\alpha$  peak is a distinctive signature of very small ceria nanoparticles (<10 nm). The integral hydrogen consumption increases strongly when the particle size of CeO<sub>2</sub> decreases (Fig. S2c). This is in line with the earlier finding that small ceria nanoparticles are more reducible in this temperature range due to the enhanced surface-to-volume ratio (28).

### Time-on-stream behavior of PdFSP samples

The catalysts were stabilized for ~14 h on stream prior to reaction rate measurements to ensure sufficiently low (<10%) and stable CO conversion levels. As shown in Fig. S30, the initial decay of CO oxidation activity is very different for small, medium and large PdFSP sample. The rate of the activity loss (indicated by the slopes  $k_1$ ,  $k_2$ ,  $k_3$ ) is the highest for large PdFSP, followed by medium and small PdFSP. To better understand the differences in time on stream behavior of the samples, we employed in situ DRIFTS. The catalysts were pretreated at 300 °C in 20% O<sub>2</sub> in He, cooled to 75 °C, and the feed was switched to a mixture of 1%CO+1%O<sub>2</sub> in He (total flow 100 ml/min) (Fig. S31). The intensity of the gas-phase CO<sub>2(g)</sub> band in the IR spectrum of large PdFSP evidences its highest activity after 5 min of reaction (mind the different scale in IR data plots) as compared to other samples, in line with the time-on-stream data (Fig. S30) and light-off tests (Fig. S20). We explain the initial high activity of large PdFSP by the presence of single-atom Pd-O species, characterized by the intense 2143 cm<sup>-1</sup> band (38, 36, 31). After 40 min on stream, these species almost entirely disappear, likely due to their reduction and sintering. As a result the IR spectra are dominated by carbonyls of suboxidized and metallic Pd clusters (2089 and ~1900 cm<sup>-1</sup>, respectively), while the decrease in the CO<sub>2(g)</sub> band points to a lower activity of the catalyst in this state. Reduction and sintering of highly dispersed Pd-O species is a common cause of activity loss in low-temperature CO oxidation (53, 38, 36, 31).

In contrast to large PdFSP, single-atom Pd-O species in small PdFSP are much more stable, even after 90 min on stream (Fig. S31). Thus, the initial decay of the activity (indicated by the decreasing CO<sub>2(g)</sub> IR band) cannot be linked to the evolution of Pd species. Several studies have shown that a decrease in CO oxidation activity of ceria-based catalysts can be caused by blockage of oxygen vacancy sites by reaction products and accumulation of carbonate and formate surface species (54, 55, 56). As shown in Fig. S31, small PdFSP is particularly prone to accumulation of (hydro)carbonates likely due to the abundance of surface oxygen vacancies (related to the high surface area) and the different redox properties. Recently, in a combined theoretical and experimental approach, Kim et al. showed that deactivation of single-atom Pd/CeO<sub>2</sub> catalysts can be linked to removal of surface oxygen atoms of ceria lattice (33) activated by adjacent Pd sites. Accordingly, we speculate that the removal of oxygen atoms from ceria lattice and accumulation of surface carbonates are the likely reasons for the slower loss of the activity of small PdFSP as compared to large PdFSP (Fig. S30). For the latter case, reduction and clustering of highly dispersed Pd-O species is a major reason for the fast decay in the activity.

DRIFTS spectra of medium PdFSP (Fig. S31) suggest partial reduction and clustering of Pd species. We propose that the intermediate rate of activity loss of medium PdFSP (Fig. S30) is due to a combination of two processes: (i) partial reduction of Pd-O species and (ii) lattice oxygen removal accompanied by accumulation of surface carbonates. It is important to note that the reaction rate studies of PdFSP samples were performed after ~14 h on stream to ensure stable and low conversion levels, as well as to capture the intrinsic difference in kinetics of CO oxidation over the catalysts.

### Results of the Rietveld refinement

In Table S8, we summarized the unit cell parameters for the CeO<sub>2</sub> supports as well as the PdFSP and PdFSPimp samples obtained from Rietveld refinement of synchrotron-based XRD data (Fig. S5). Regardless of the preparation method, we see only a slight decrease of the lattice parameter with an increasing size of the ceria particles. This can be caused by the lower number of local defects and lower concentration of Ce<sup>3+</sup> ions in the lattice of larger particles and their higher crystallinity (57). When comparing lattice parameters of similar-sized CeO<sub>2</sub> and Pd/CeO<sub>2</sub> samples prepared by one-step FSP and by impregnation, no evidence of significant lattice expansion/contraction was found. Substitution of Ce<sup>4+</sup> ions by ions with smaller ionic radii (such as Pd<sup>2+</sup>) can cause the contraction of the ceria lattice (58, 59). However, substitution of a 4+ ion by a 2+ ion leads to Ce<sup>3+</sup> ions to retain the electroneutrality of the lattice. These Ce<sup>3+</sup> ions cause the expansion of the ceria lattice (60, 61). The minor changes in the lattice parameter, observed in this work, are likely caused by the superposition of these two counteracting effects. This hypothesis can also explain the controversial results reported in literature: both contraction (58, 59) and expansion of the ceria lattice by introduction of Pd ions (62, 63) have been reported. Finally, we note that also sample displacement, not uncommon for lab-based powder XRD measurements recorded in the Bragg-Brentano geometry, can also cause notable shifts of diffraction peaks, and may thus be another reason for the discrepancies in the literature (64).

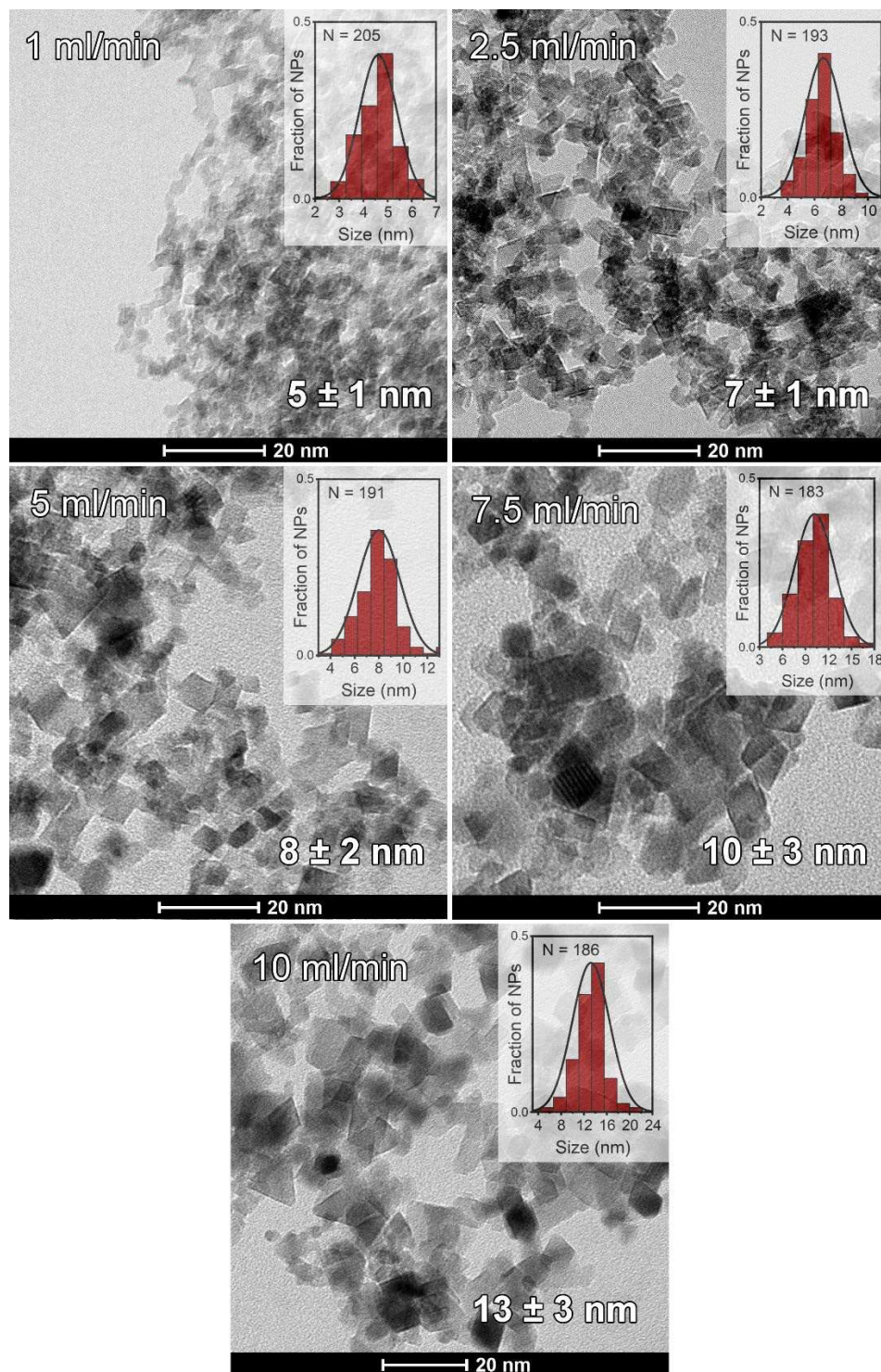


**Fig. S1. Bright-field STEM images and particle size distribution plots.** CeO<sub>2</sub> nanoparticles were prepared by FSP with different injection rate of the liquid precursor (1 to 10 ml/min).

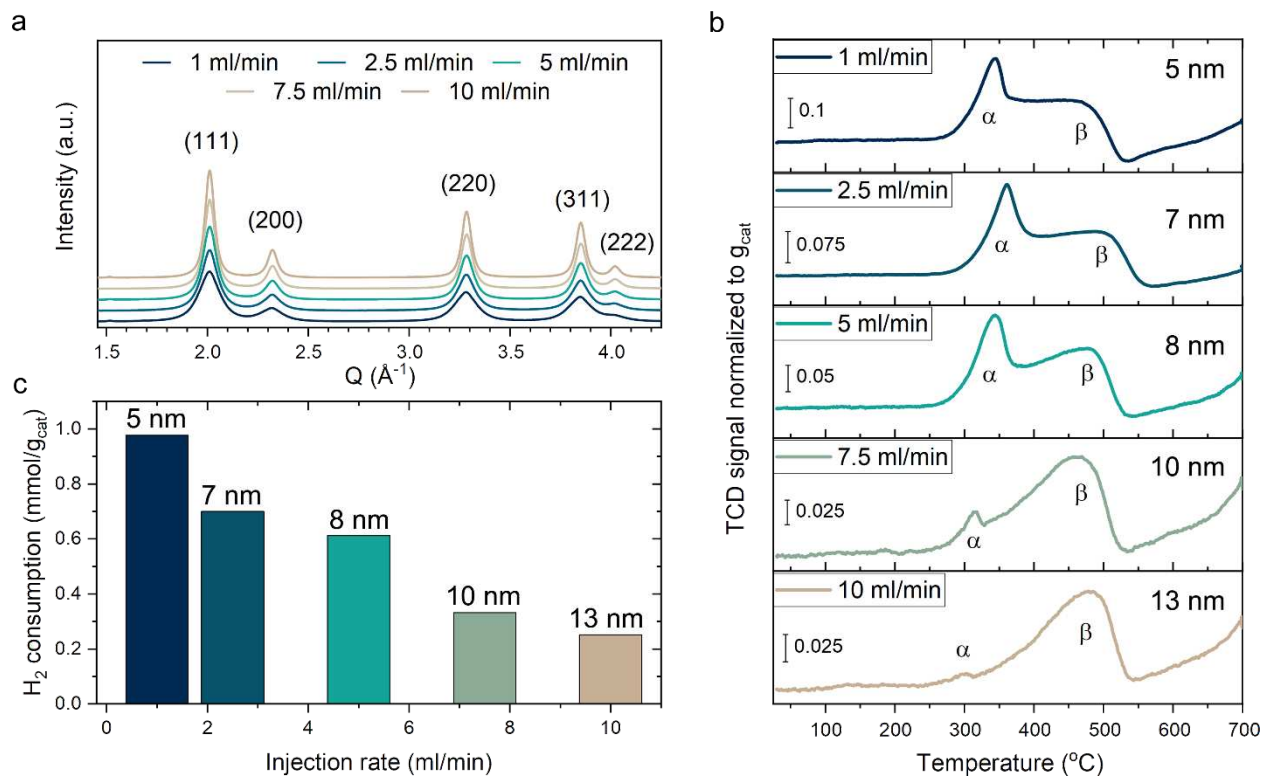


**Fig. S2. Characterization of  $\text{CeO}_2$  powders prepared by FSP with variable injection feed rate of the liquid precursor (1 to 10 ml/min).** a) Synchrotron powder XRD patterns acquired at  $\lambda = 0.18233 \text{ \AA}$ . b)  $\text{H}_2$ -TPR profiles of fresh FSP- $\text{CeO}_2$  prepared at different injection rates. c) Quantification of  $\text{H}_2$  consumption (250-550  $^\circ\text{C}$ ) for the FSP- $\text{CeO}_2$  supports. As mentioned in the supplementary text, the size of ceria NPs affects the redox properties as observed by  $\text{H}_2$ -TPR.

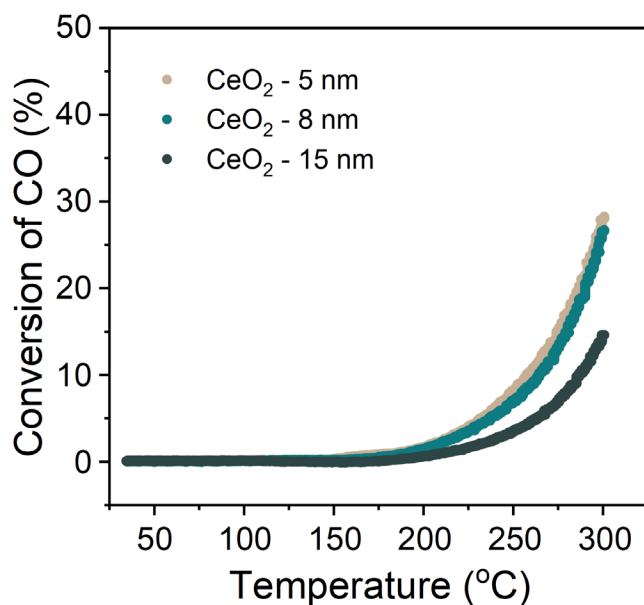


**Fig. S3. CO oxidation light-off curves for FSP-made CeO<sub>2</sub> supports of different size.** The temperature ramp up was performed from 30 to 300 °C at a rate of 5 °C/min. The ramp down curve was measured during unrestrained cooling of the furnace overnight. Reaction conditions: 1% CO and 1% O<sub>2</sub> in He (GHSV ~180,000 ml gcat<sup>-1</sup> h<sup>-1</sup>). Ceria nanoparticles without Pd do not display low-temperature CO oxidation activity (<100 °C). At elevated temperature (>200 °C), small (5 nm) and medium (8 nm) nanoparticles are more active than larger ones (15 nm, comparable to commercial ceria), which can be explained by the lower surface area of the latter.

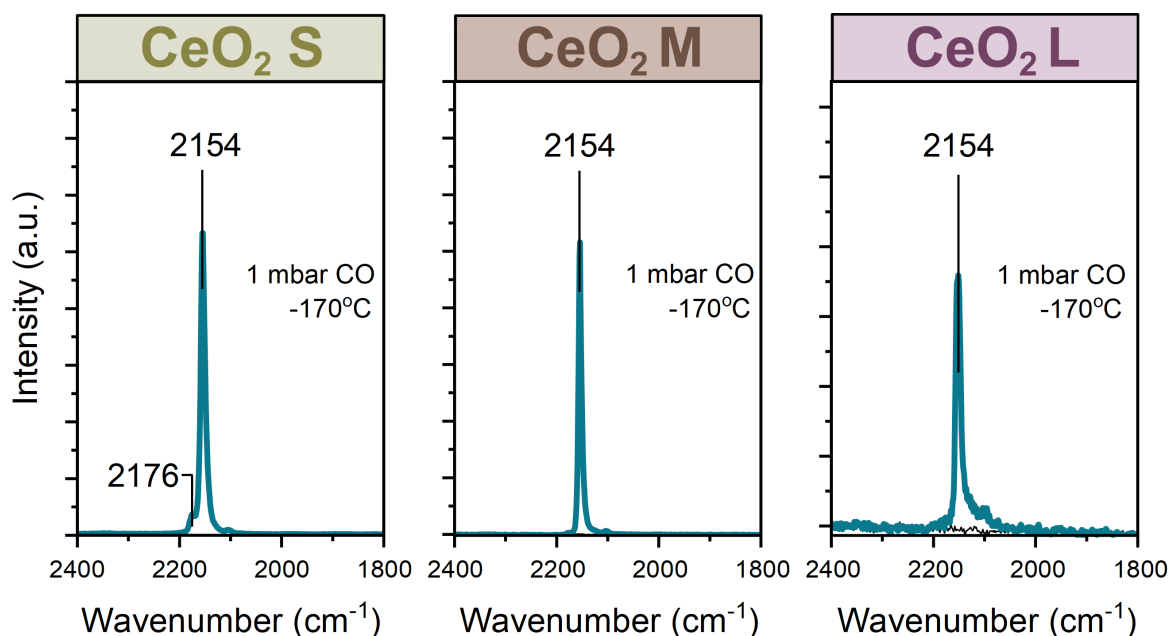


**Fig. S4. Transmission FTIR spectra of fresh catalysts collected during CO adsorption at -170 °C.** The samples were first pretreated in O<sub>2</sub> at 300 °C and then cooled down to RT and evacuated. Further cooling was performed via circulation of liquid nitrogen within the sample holder. After reaching -170 °C CO was dosed up to a pressure of 1 mbar. the major IR band located at 2154 cm<sup>-1</sup> in all samples corresponds to CO adsorbed on Ce<sup>4+</sup> sites of (111) CeO<sub>2</sub> facets (65, 66). In the spectrum of small CeO<sub>2</sub> only a minor contribution of 2176 cm<sup>-1</sup> band can be observed, which may be attributed to CO adsorbed on Ce<sup>3+</sup> sites of (111) CeO<sub>2</sub> and/or on (110)-terminated CeO<sub>2</sub> surfaces (65, 66). Based on these data we conclude that CeO<sub>2</sub> nanoparticles prepared by FSP predominantly expose the most thermodynamically stable (111) surfaces.

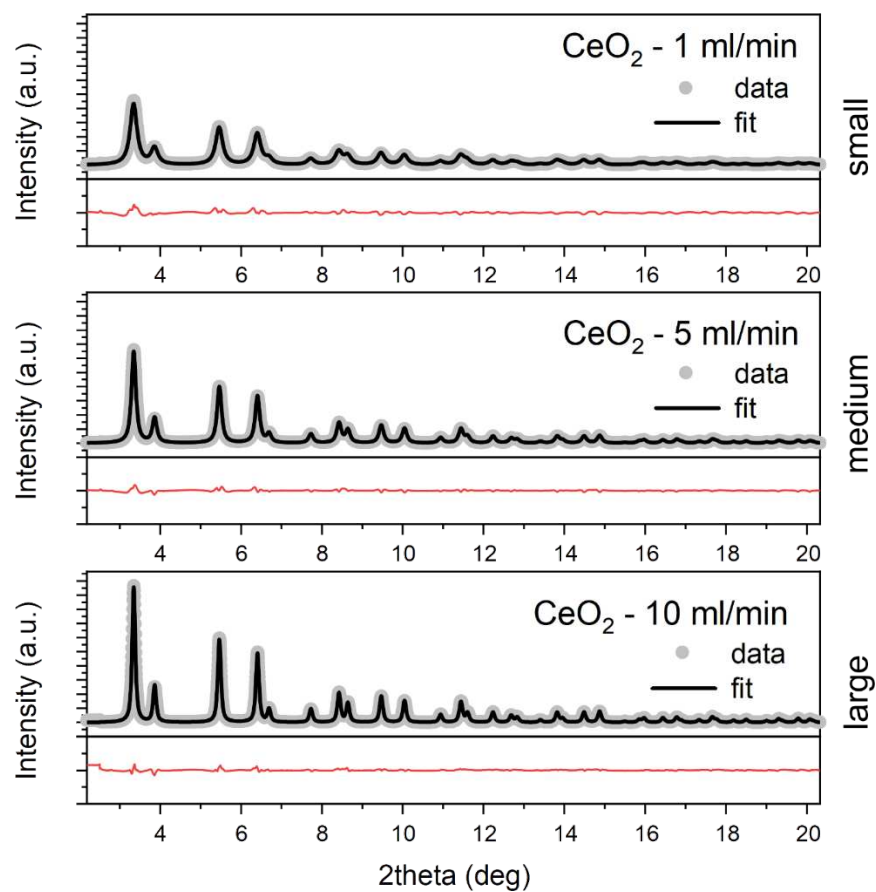


**Fig. S5.** Example of the 2theta range used for Rietveld refinement of synchrotron-based ( $\lambda = 0.18233 \text{ \AA}$ ) XRD data obtained in Debye-Scherrer geometry.

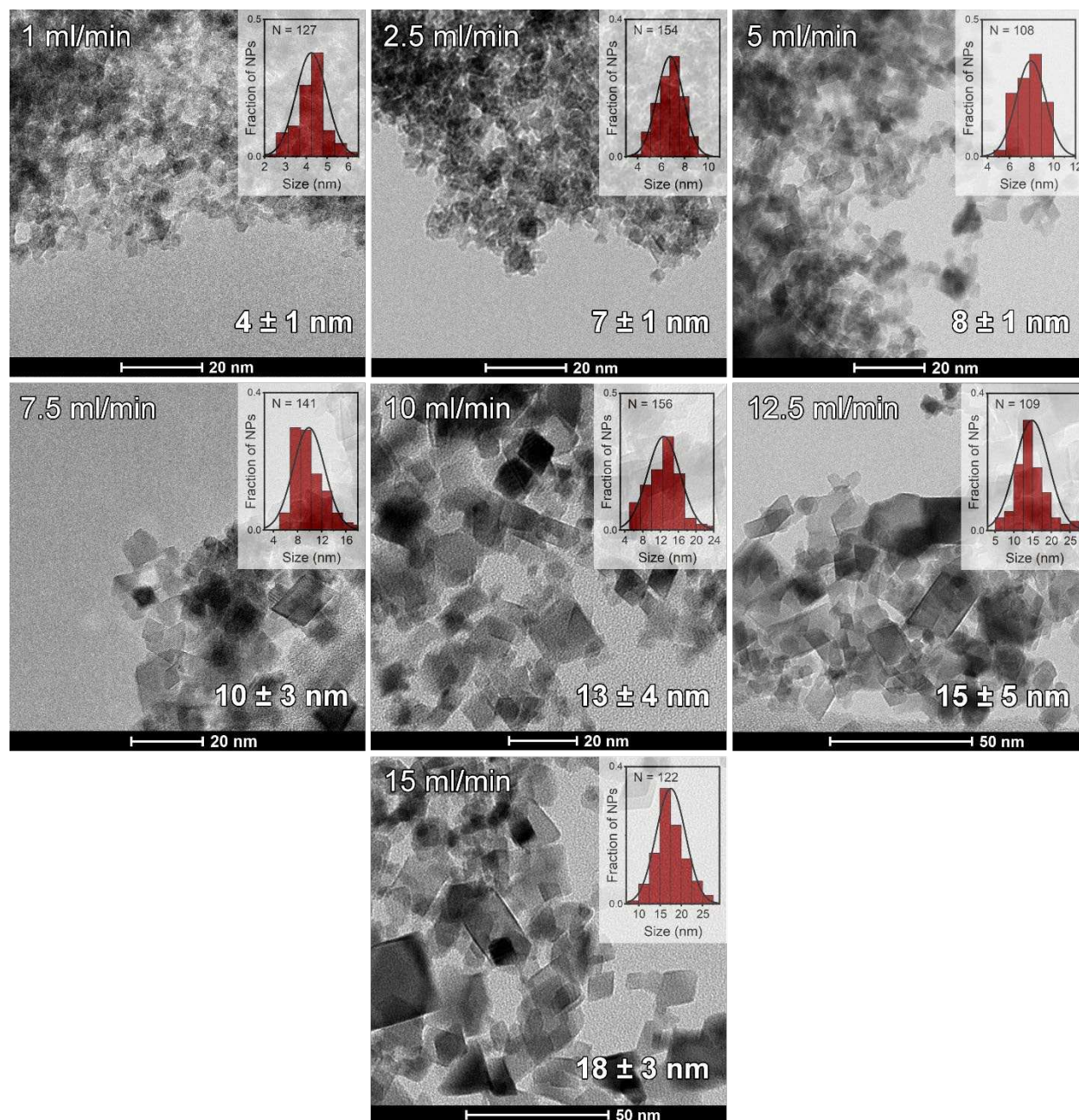


**Fig. S6. Bright-field STEM images and particle size distribution plots.** 1 wt% Pd/CeO<sub>2</sub> nanoparticles (PdFSP) were prepared by one-step FSP (mixture of Pd and Ce precursors) with different injection rate of the liquid precursor (1 to 15 ml/min). The size of PdFSP NPs increases with the injection rate and the particle size distribution broadens.

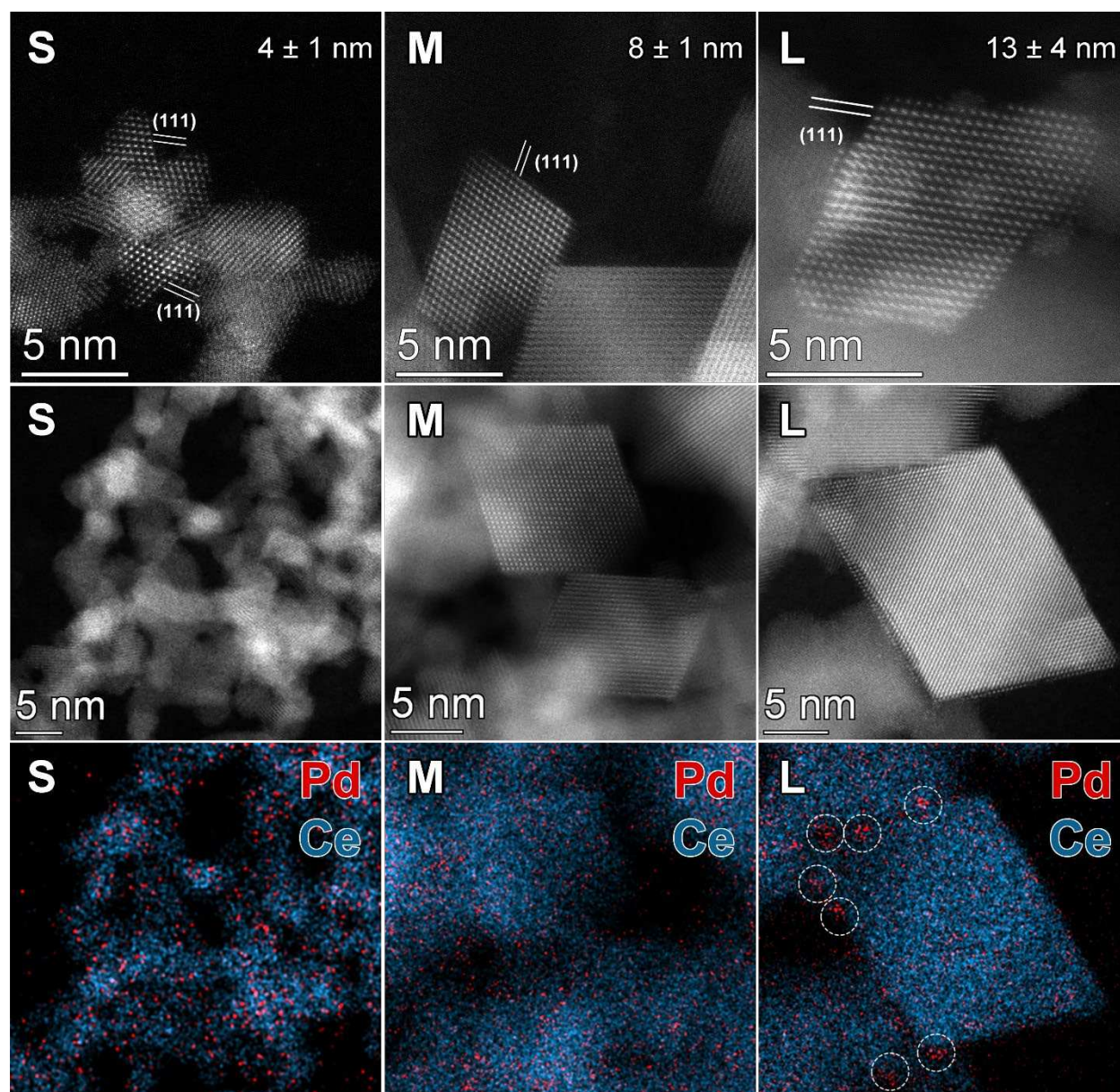


**Fig. S7. HAADF STEM imaging and EDX elemental mapping of PdFSP samples.** Labels “S”, “M” and “L” refer to catalysts with small (~4 nm), medium (~8 nm) and large (~13 nm) size of CeO<sub>2</sub>, respectively. Ceria particles are predominantly (111) faceted. On small and medium PdFSP, no Pd/PdO NPs were discerned and Pd is homogeneously distributed over the support. On large PdFSP some small clusters (< 2 nm) can be detected alongside highly dispersed Pd.

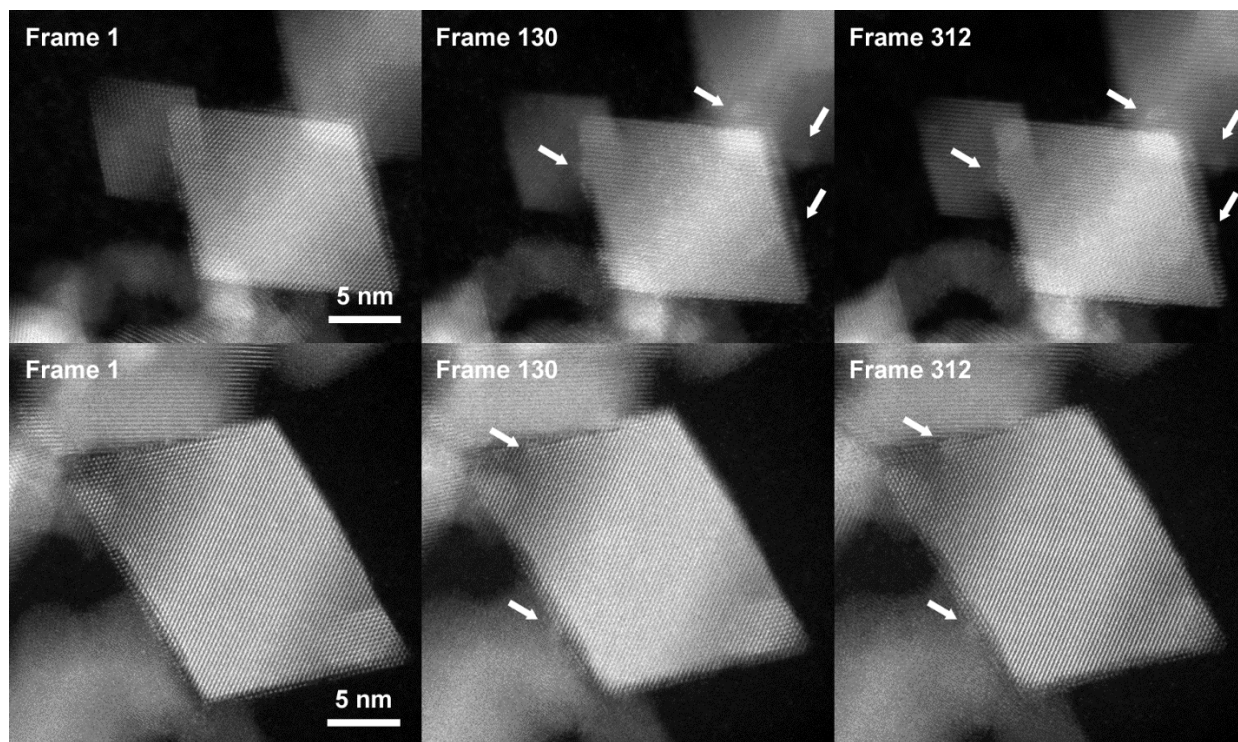


**Fig. S8. HAADF STEM imaging of large PdFSP sample.** Prolonged electron beam exposure causes Pd migration and agglomeration in to larger NPs.

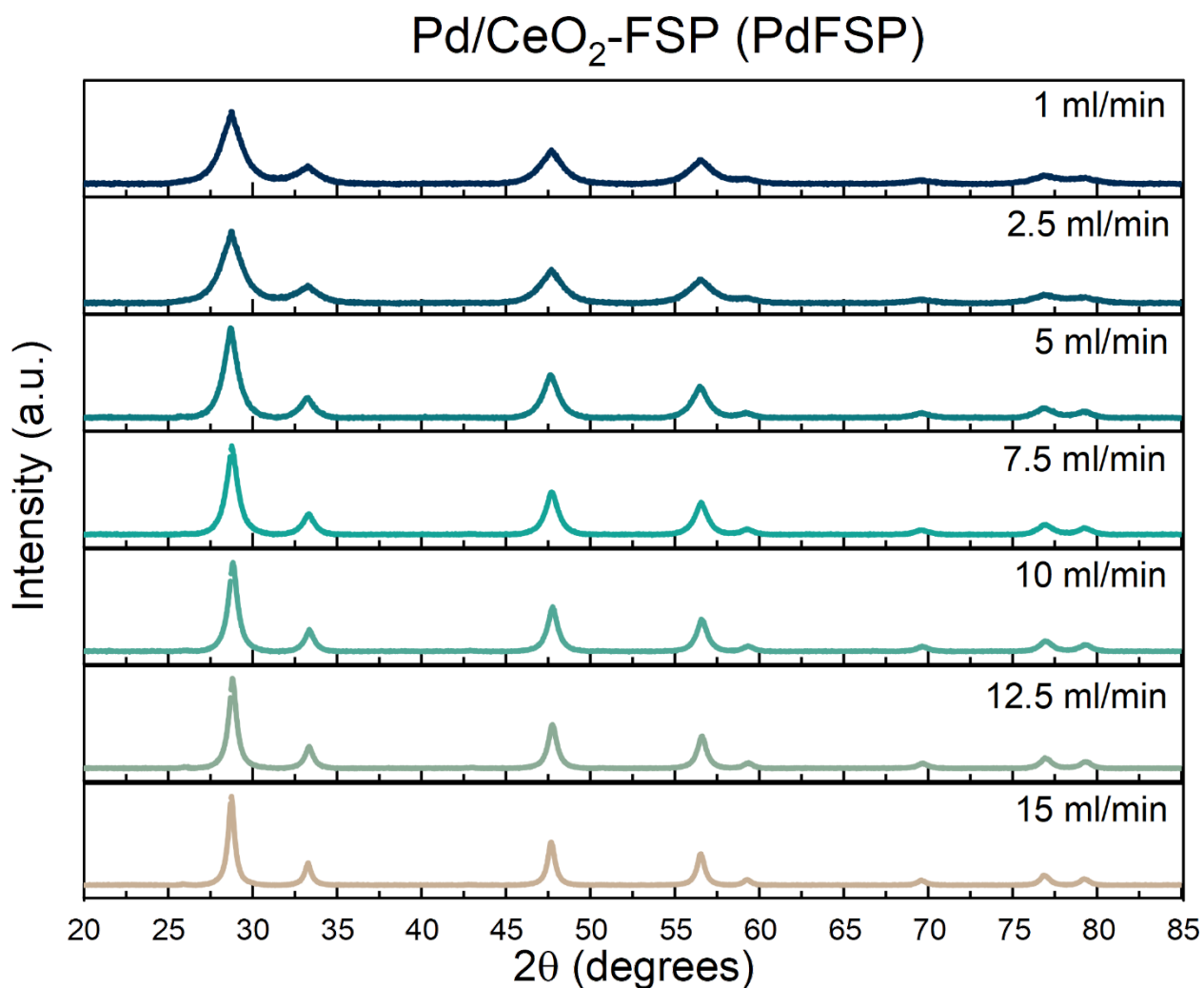


**Fig. S9. XRD patterns of PdFSP samples prepared at different injection rate.** Increase of the injection rate during FSP leads to narrowing of ceria diffraction peaks in line with the increase of crystallite size. Diffraction peaks related to bulk Pd/PdO phases cannot be discerned.

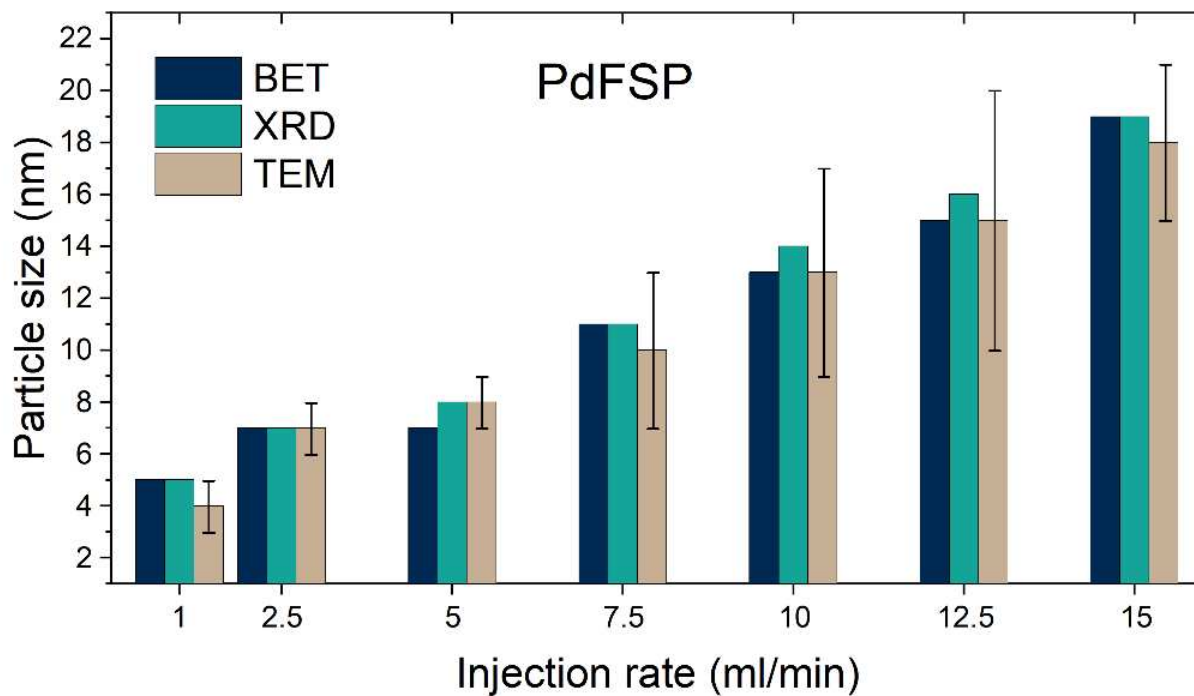


**Fig. S10. Particle sizes of PdFSP determined by different methods.** Good agreement between XRD (Scherrer equation), physisorption (BET) and TEM data was found.

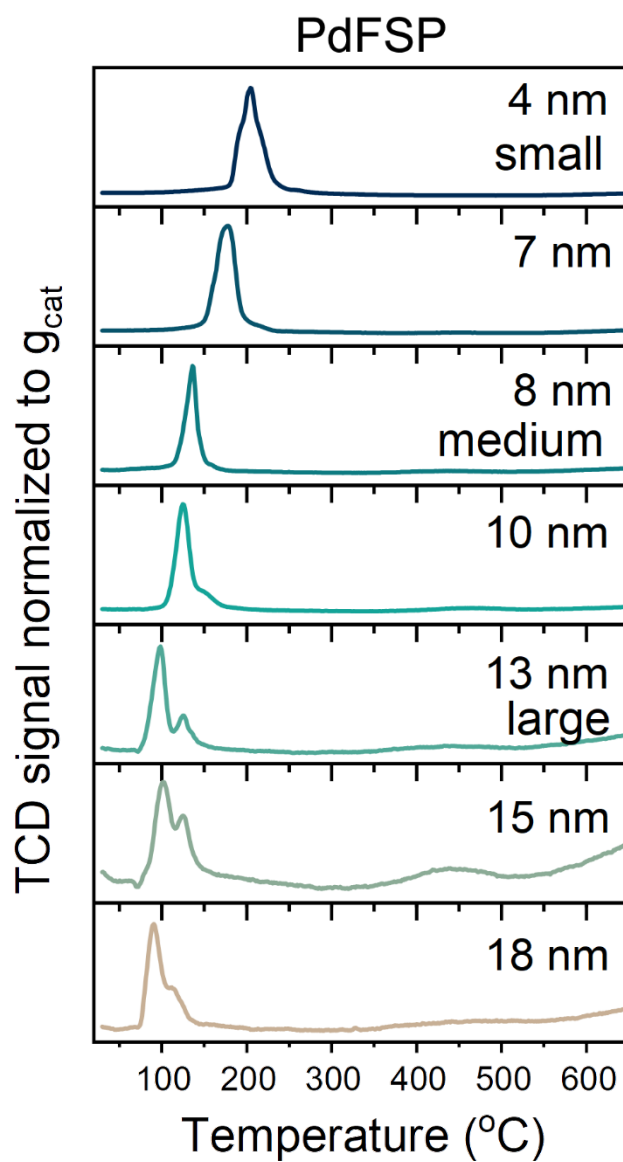


**Fig. S11. H<sub>2</sub>-TPR profiles for PdFSP samples.** As the particles of the support increase in size, MSI between palladium and ceria weakens, which results in the shift of reduction peak to lower temperature.

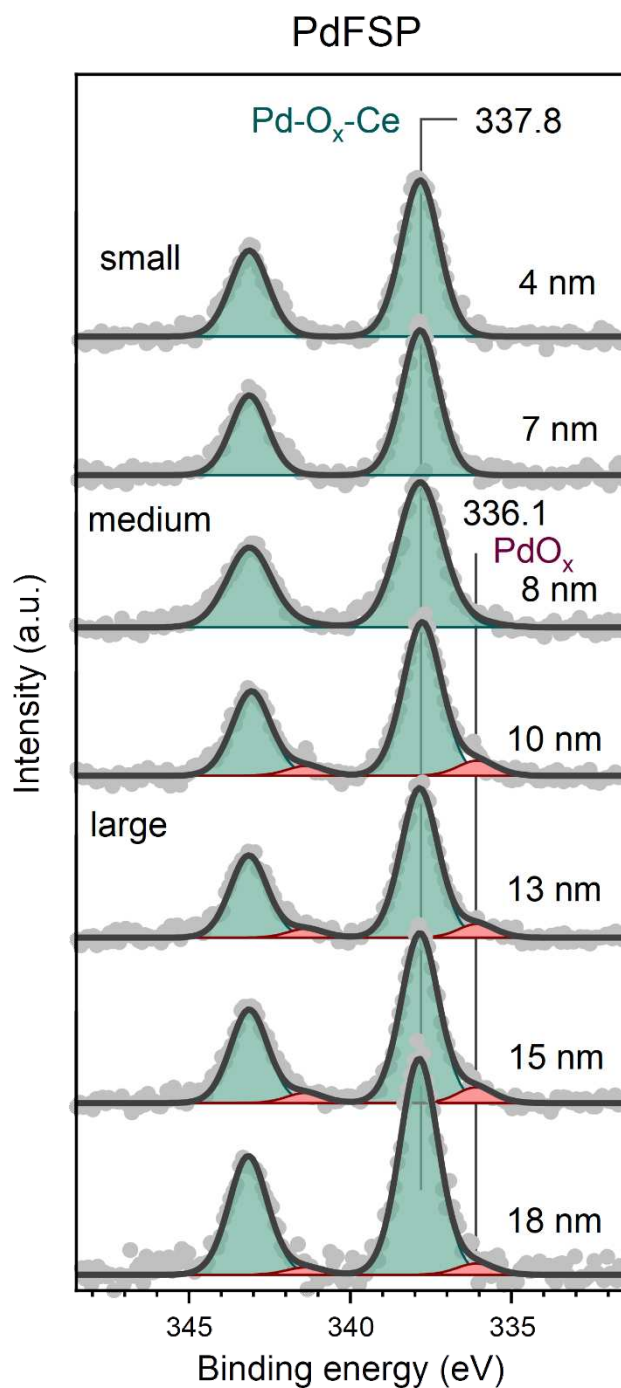


**Fig. S12. Photoelectron spectra of Pd 3d core level for PdFSP samples.** Pd 3d<sub>5/2</sub> component at 337.8 eV, attributed to highly dispersed Pd<sup>2+</sup>-O<sub>x</sub>-Ce moieties, dominates the spectra for all samples. Only for large NPs (> 10 nm) an additional component at 336.1 eV appears, which indicates the presence of a small fraction of PdO<sub>x</sub> (x<1) clusters in these samples.

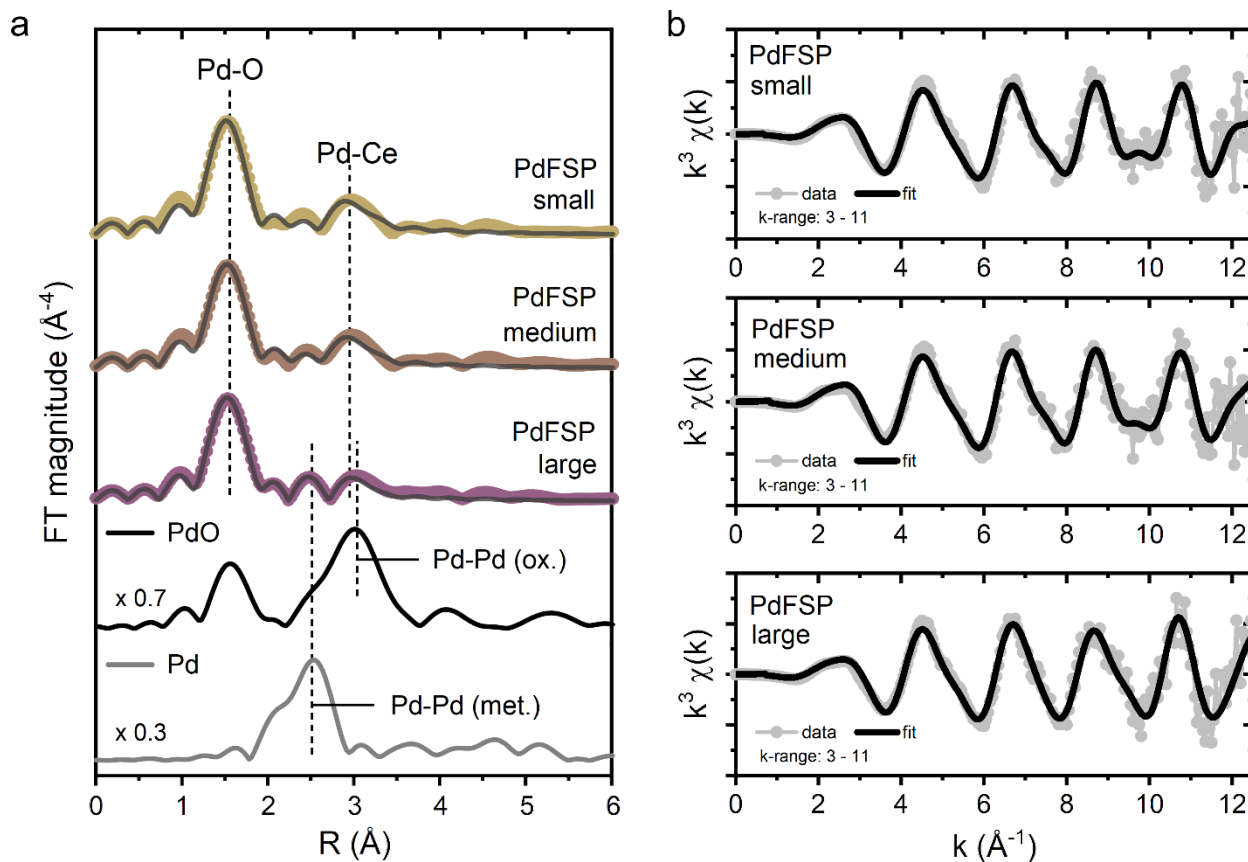


**Fig. S13. EXAFS data for PdFSP samples and reference compounds acquired at the Pd K-edge.** a) R-space  $k^3$ -weighted EXAFS. b) k-space  $k^3$ -weighted EXAFS. For large PdFSP a small contribution of Pd-Pd scattering is present.

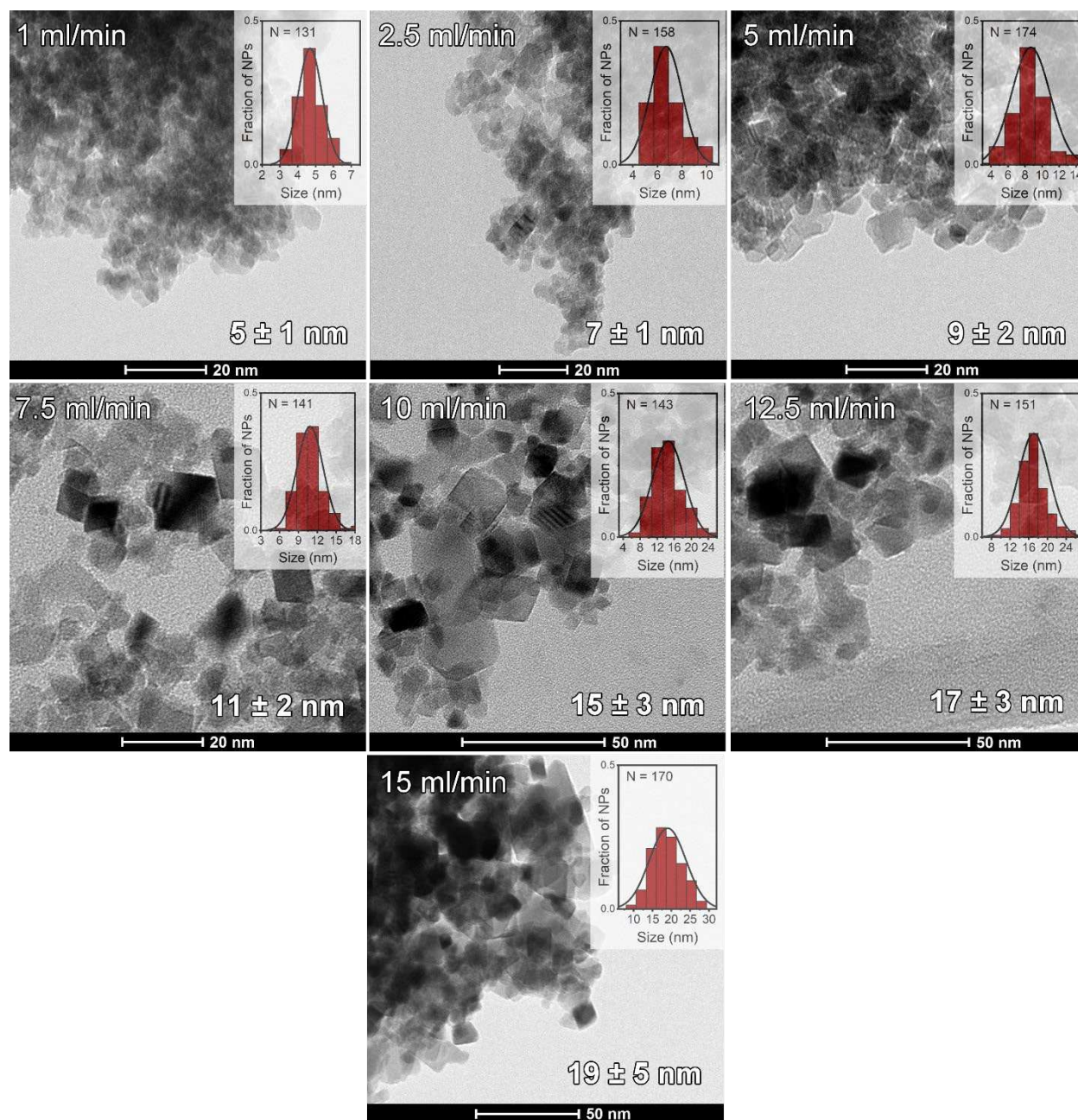


**Fig. S14. Bright-field STEM images and particle size distribution plots.** 1 wt% Pd/CeO<sub>2</sub> nanoparticles (PdFSPimp) were prepared by wet impregnation of FSP-CeO<sub>2</sub> NPs obtained with different injection rate of the liquid precursor (1 to 15 ml/min). The size of PdFSPimp NPs increases with the injection rate and the particle size distribution broadens.

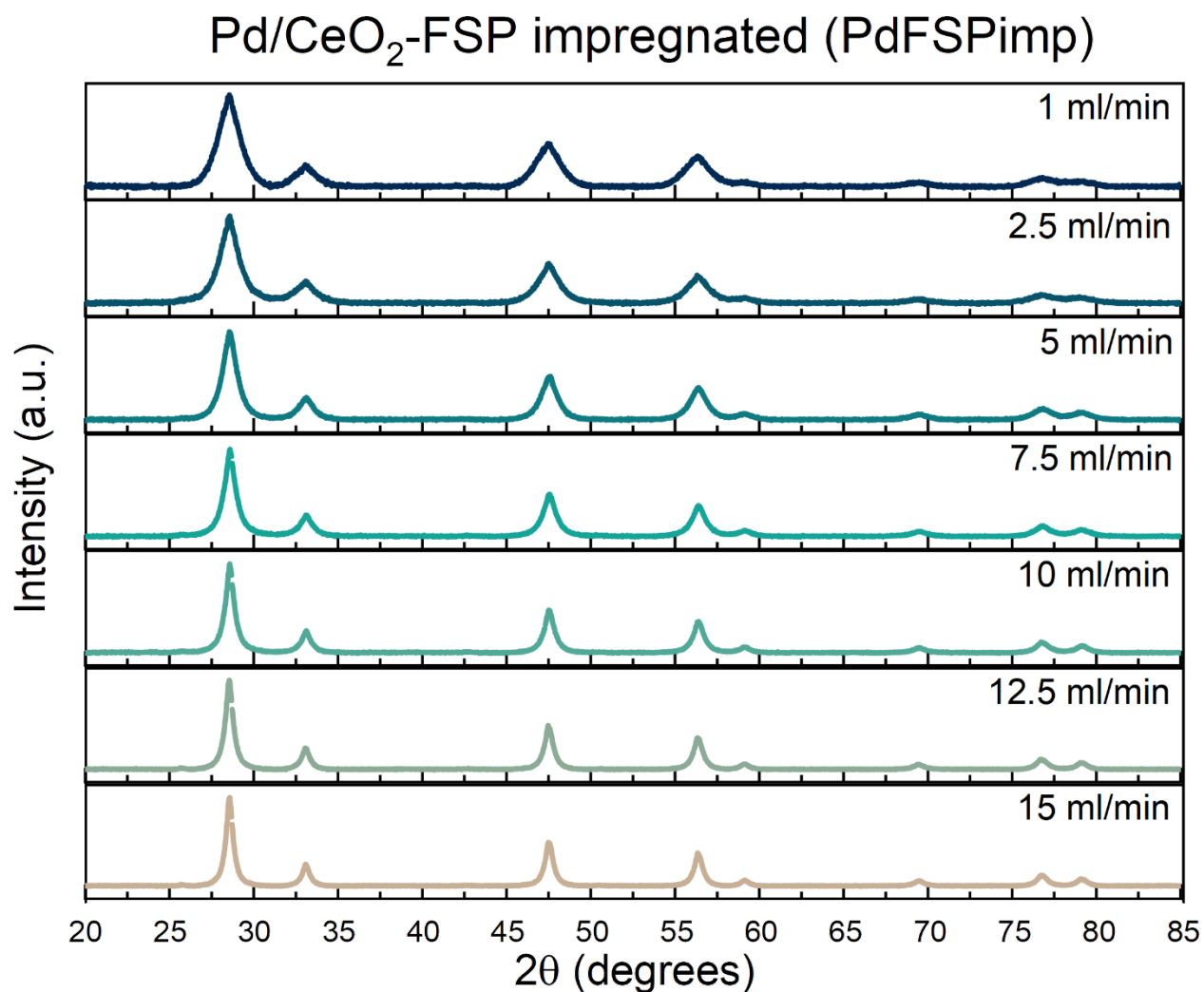


**Fig. S15.** XRD patterns of PdFSPimp samples prepared at different injection rate. Increase of the injection rate during FSP leads to narrowing of ceria diffraction peaks in line with the increase of crystallite size. Diffraction peaks related to bulk Pd/PdO phases cannot be discerned.

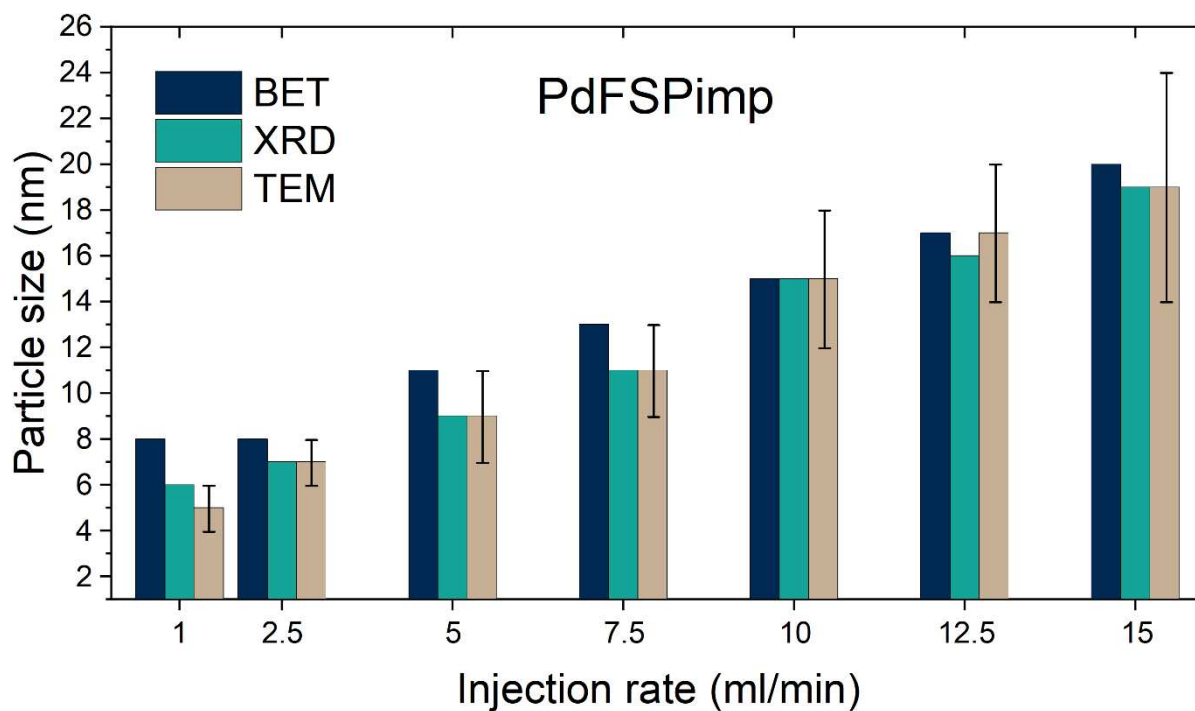


**Fig. S16. Particle sizes of PdFSPimp determined by different methods.** Good agreement between XRD (Scherrer equation), physisorption (BET) and TEM data was found. Slightly larger size of PdFSPimp NPs as compared to PdFSP may stem from the wet impregnation step followed by calcination at 300 °C.

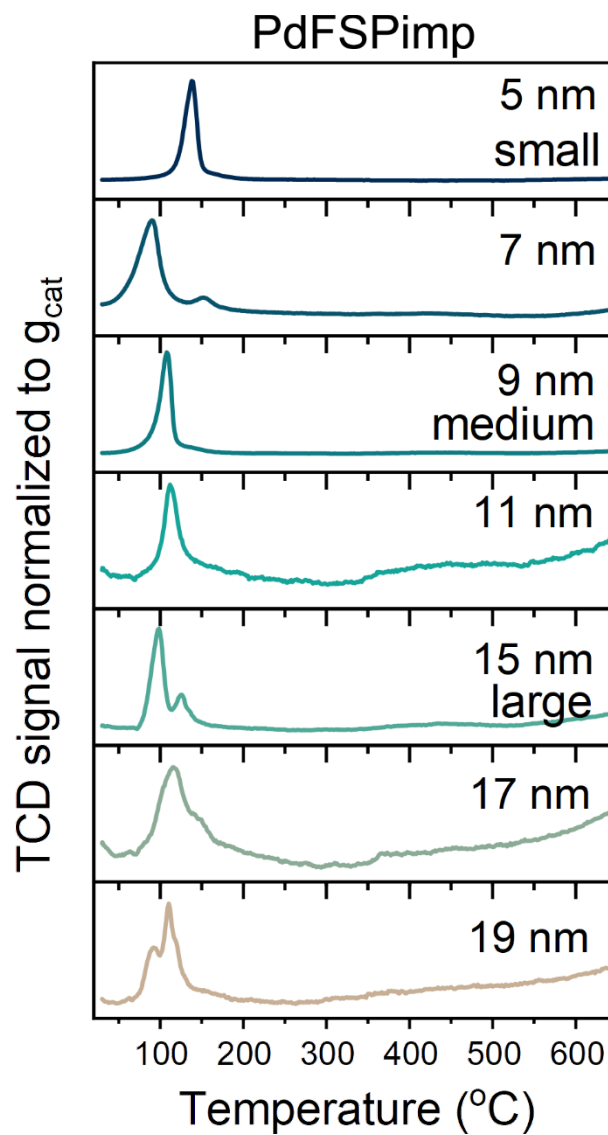


**Fig. S17. H<sub>2</sub>-TPR profiles for PdFSPimp samples.** As the particles of the support increase in size, MSI between palladium and ceria weakens, which results in the slight shift of reduction peak to lower temperature. Overall lower reduction temperatures and lower H<sub>2</sub> consumption (Table S2) with respect to PdFSP samples indicate weaker interaction between Pd and CeO<sub>2</sub> in these samples.

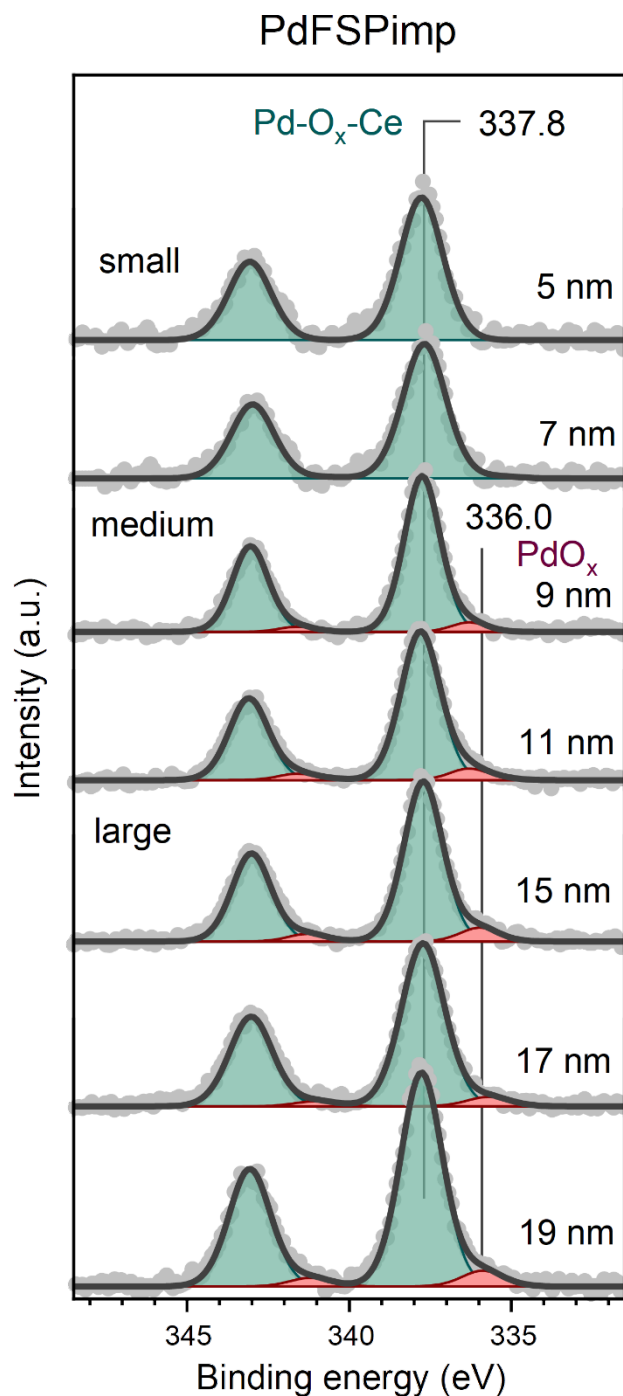


**Fig. S18. Photoelectron spectra of Pd 3d core level for PdFSPimp samples.** The supports were prepared by FSP and subsequently impregnated with 1 wt % Pd. The Pd 3d<sub>5/2</sub> component at 337.8 eV, attributed to highly dispersed Pd<sup>2+</sup>-O<sub>x</sub>-Ce moieties, dominates the spectra for all samples. In contrast to PdFSP an additional component at 336.1 eV appears already in medium PdFSPimp samples, which indicates the presence of a small fraction of PdO<sub>x</sub> (x<1) clusters. This is in line with weaker MSI in PdFSPimp concluded from H<sub>2</sub>-TPR data.

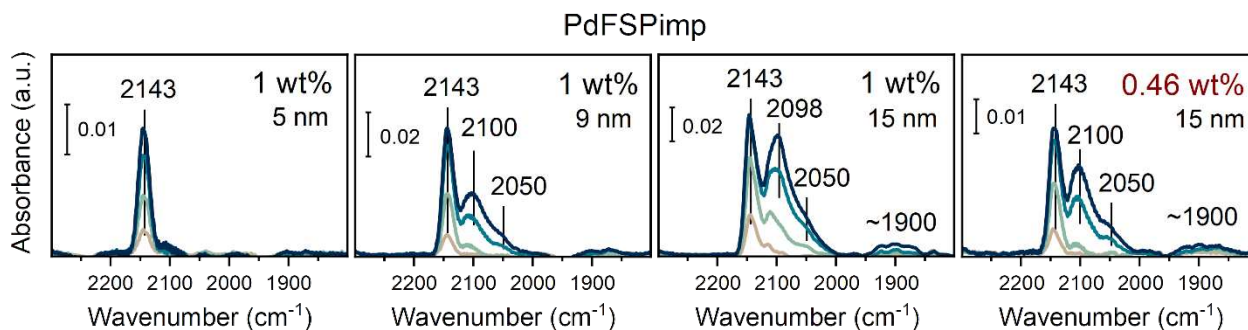


**Fig. S19. CO adsorption at -20 °C followed by in situ DRIFTS for fresh PdFSPimp samples.** Flow of CO was fixed to 0.3 ml/min yielding 2 mbar of total pressure in the in situ cell. The single-atom nature of Pd sites manifested by  $\sim 2140$   $\text{cm}^{-1}$  band in spectra of small  $\text{CeO}_2$  nanoparticles is preserved even for impregnated samples. Yet we note a slightly higher contribution of CO carbonyls related to Pd clusters in case of large nanoparticles of PdFSPimp than for PdFSP. This can be explained by the higher Pd surface concentration due to impregnation preparation method of PdFSPimp. To account for differences in Pd surface concentration, we prepared a reference sample by impregnating large  $\text{CeO}_2$  with a lower Pd loading (0.46 wt%) to reach the amount of Pd per unit of surface area (based on BET surface area analysis) as for the small nanoparticles. Although the overall intensity of CO bands decreased due to the lower concentration of Pd (see scale bars), some agglomerated Pd species ( $\sim 2050$  and  $\sim 1900$   $\text{cm}^{-1}$  bands) are still observed. Thus, we infer that weaker MSIs are the major cause of the lower stability of Pd single atoms on large  $\text{CeO}_2$  instead of differences in the Pd surface concentration.

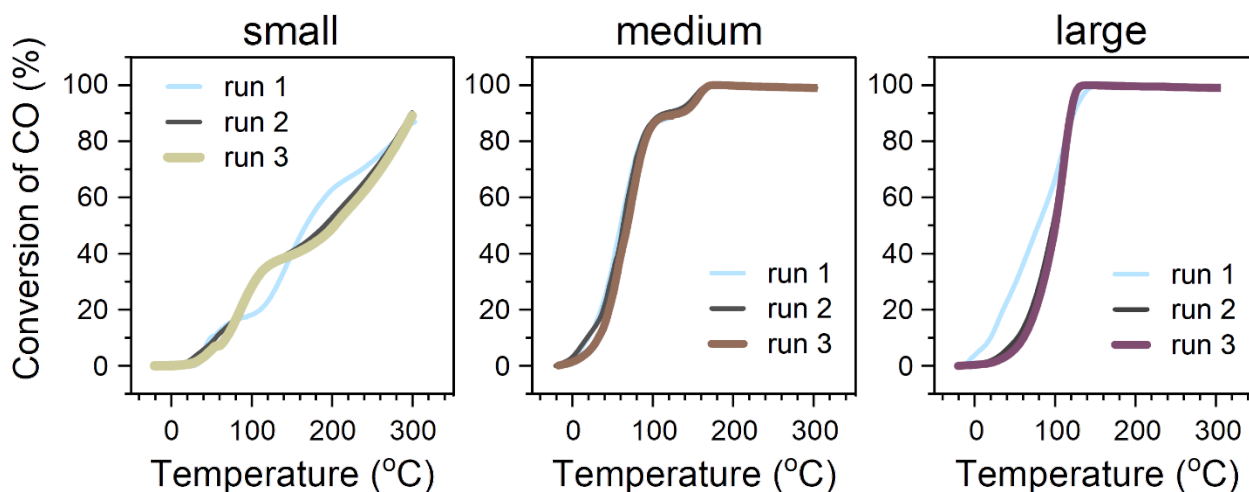


**Fig. S20. Consecutive CO oxidation light-off curves for small, medium, and large PdFSP samples.** The temperature ramp was performed from to -20 to 300 °C at a heating rate of 5 °C/min. Reaction conditions: 1% CO and 1% O<sub>2</sub> in He (GHSV ~180,000 ml g<sub>cat</sub><sup>-1</sup> h<sup>-1</sup>). Three consecutive light-off runs were performed.

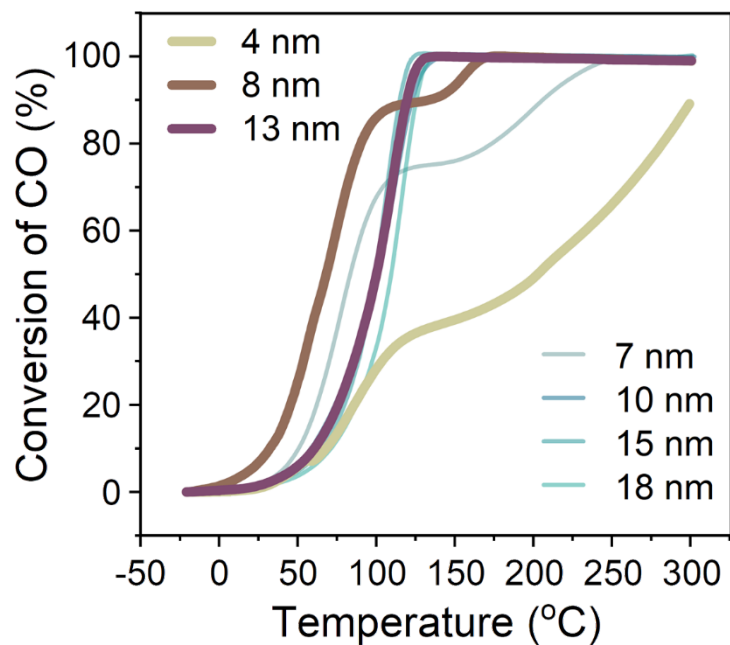


**Fig. S21. CO oxidation light-off curves for PdFSP samples of different size.** The temperature ramp was performed from -20 to 300 °C at a heating rate of 5 °C/min. Reaction conditions: 1% CO and 1% O<sub>2</sub> in He (GHSV ~180,000 ml g<sub>cat</sub><sup>-1</sup> h<sup>-1</sup>). Three consecutive light-off test were performed, and the third run is shown in the figure. Clearly the CO oxidation strongly differs as a function of PdFSP size.

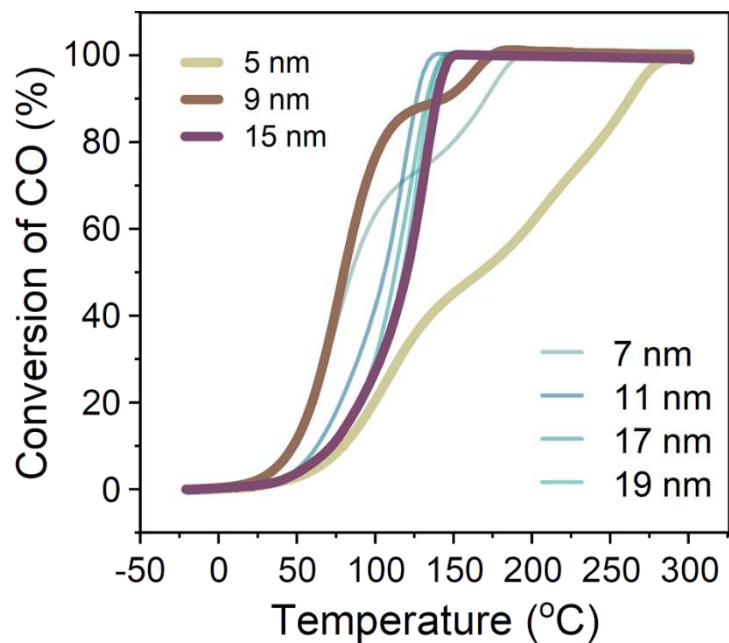


**Fig. S22. CO oxidation light-off curves for PdFSPimp samples of different size.** The temperature ramp was performed from -20 to 300 °C at a heating rate of 5 °C/min. Reaction conditions: 1% CO and 1% O<sub>2</sub> in He (GHSV ~180,000 ml g<sub>cat</sub><sup>-1</sup> h<sup>-1</sup>). Three consecutive light-off tests were performed, and the third run is shown in the figure. Clearly the CO oxidation strongly differs as a function of PdFSPimp size similarly to PdFSP catalysts. Overall PdFSPimp samples exhibit worse low-temperature CO oxidation activity than PdFSP of similar size. This may stem from the lower Pd dispersion in PdFSPimp as evidenced by DRIFTS (Fig.S19).

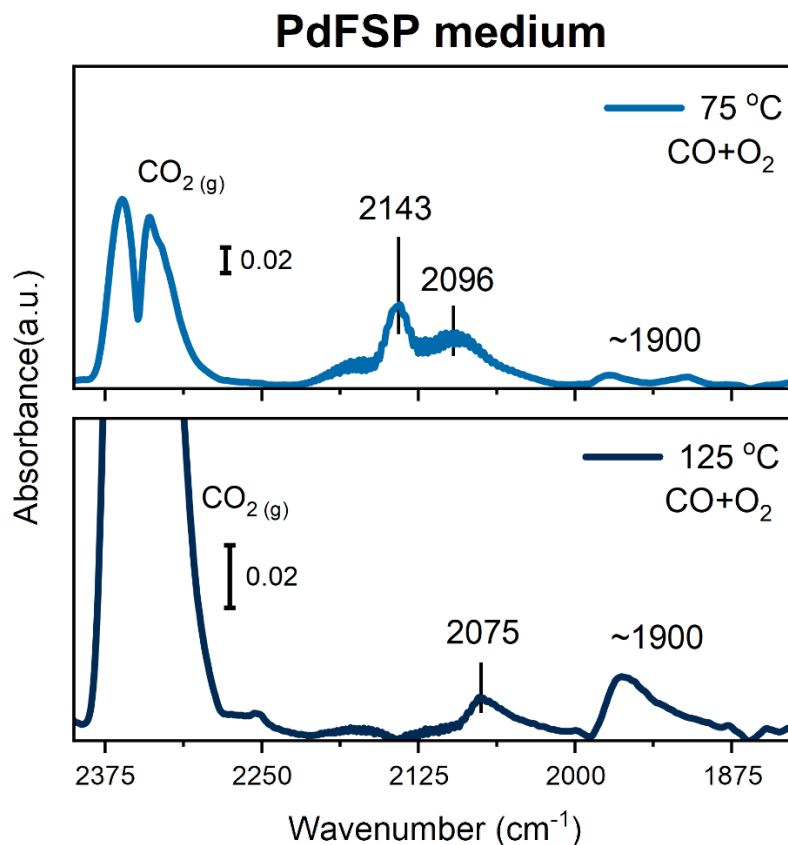


**Fig. S23. In situ DRIFTS spectra of medium PdFSP.** The spectra were acquired during CO oxidation at 75 °C and 125 °C in reaction mixture (1% CO and 1% O<sub>2</sub> in He, total flow 100 ml/min). The absence of the band related to CO adsorbed on atomically dispersed Pd species ( $\sim 2140\text{ cm}^{-1}$ ) at elevated temperature points to their weaker adsorption with respect to linear- and bridge-bonded CO on metallic Pd ( $\sim 2075\text{ cm}^{-1}$  and  $\sim 1900\text{ cm}^{-1}$ , respectively). Importantly, the high-frequency band related to Pd single atoms is evident in the spectra of the small and medium PdFSP after the reaction at 300 °C (Fig. 3(C)) confirming that the absence of  $\sim 2140\text{ cm}^{-1}$  band at elevated temperature stems from the reaction/desorption of CO rather than from instability of atomically dispersed Pd species.

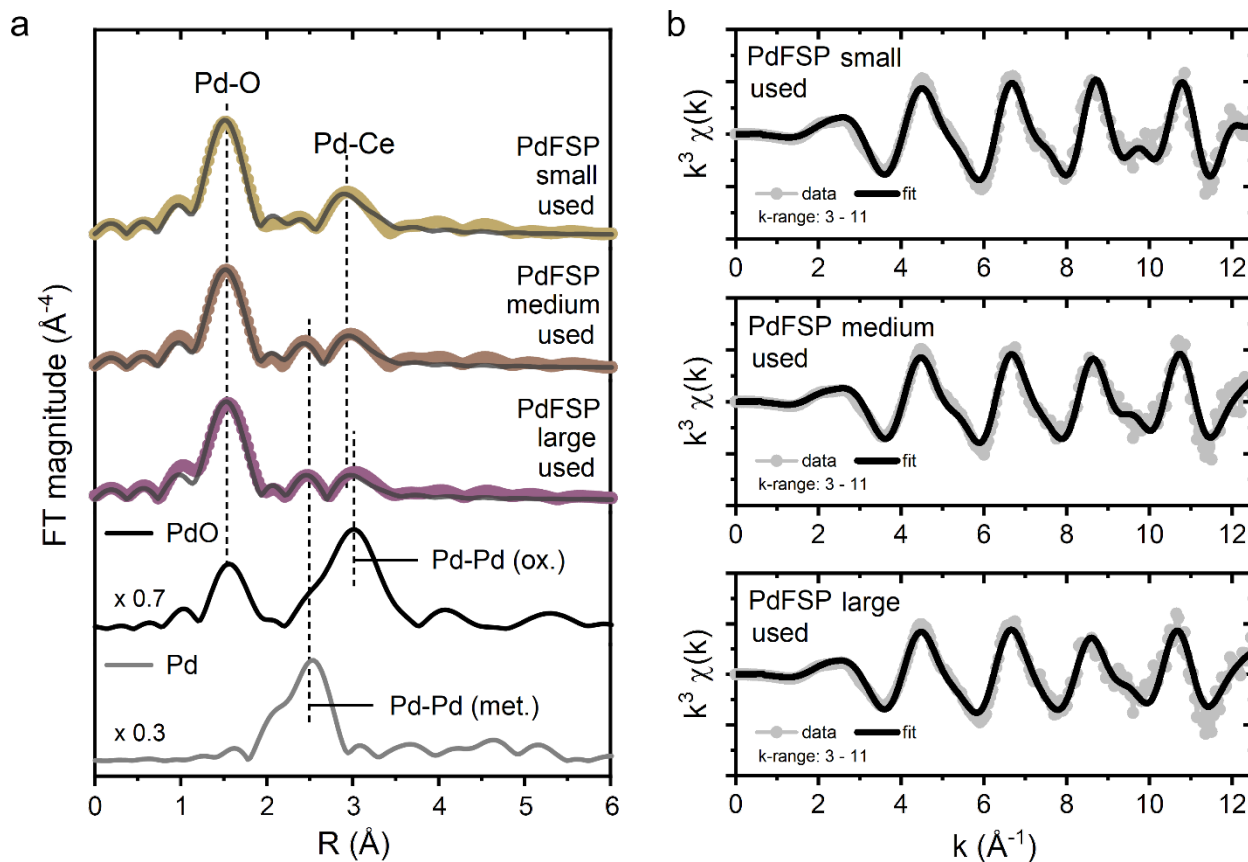


**Fig. S24. EXAFS data for used PdFSP samples and reference compounds acquired at the Pd K-edge.** a) R-space  $k^3$ -weighted EXAFS. b) k-space  $k^3$ -weighted EXAFS. The data is acquired for the samples exposed to reaction mixture (1% CO and 1% O<sub>2</sub> in He, total flow 100 ml/min) at 300 °C during DRIFTS experiments shown in Fig. 3(C). For used medium and large PdFSP catalysts the presence of a small contribution of Pd-Pd scattering is accompanied by a slight decrease in Pd-O CNs with respect to fresh samples (Table S3). This goes in line with partial clustering of Pd under reaction conditions evidenced by DRIFTS (Fig. 3(C)).

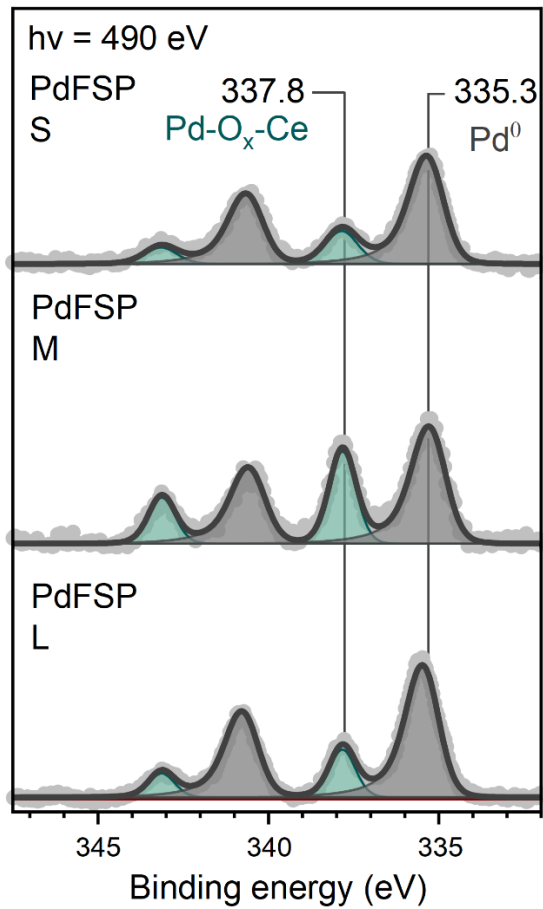


**Fig. S25. Synchrotron radiation based in situ NAP-XPS data.** Pd 3d spectra of the catalysts exposed to 1 mbar CO at 175 °C. Spectra were acquired at 490 eV, corresponding to an inelastic electron mean free path (IMFP) of ca. 5 Å. In all samples reduction of Pd-oxo species to Pd<sup>0</sup> (335.3 eV) is incomplete under such conditions and the spectral component at 337.8 eV related to Pd<sup>2+</sup>-O-Ce moieties remains visible. Stabilization of Pd<sup>2+</sup> in strong interaction with ceria is most notable for medium PdFSP sample.

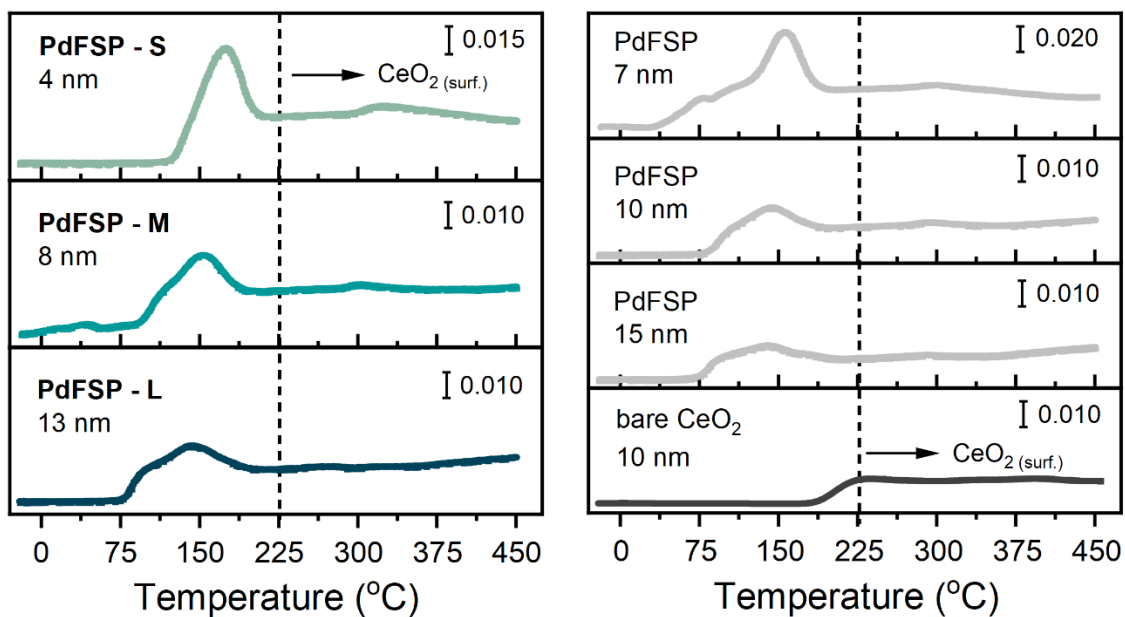


**Fig. S26. TPR-CO data.** As follows from the TPR curves, the extent of reduction by CO depends on the size of PdFSP samples. The low temperature region (<200 °C) is related to reduction of both Pd<sup>2+</sup> and Ce<sup>4+</sup> species as follows from Pd 3d (Fig. S25) and valence band RPES spectra (Fig. 4(A)).

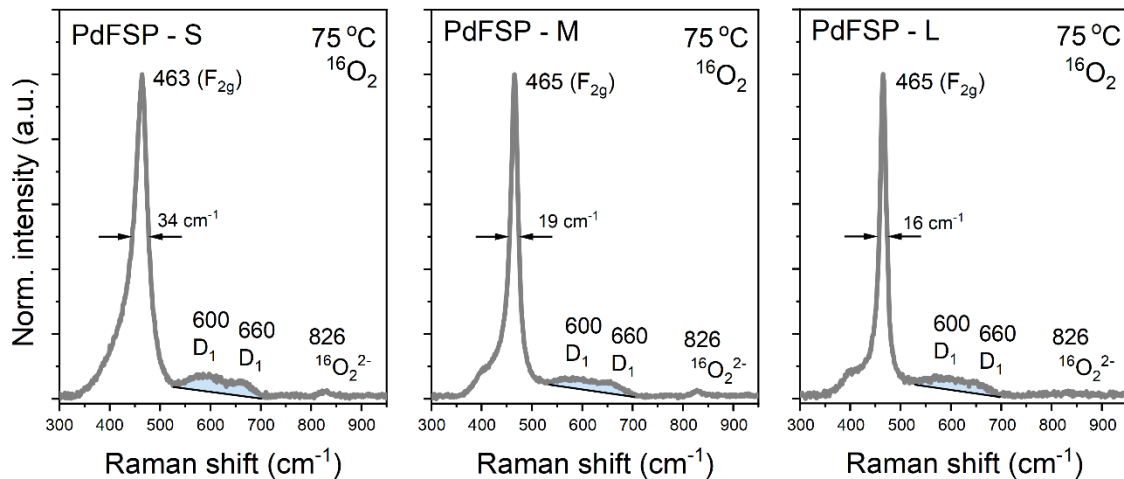


**Fig. S27. Normalized in situ Raman spectra.** The relative intensity of D-band, including extrinsic and intrinsic defects, and the width of F<sub>2g</sub> band increase following the decrease in PdFSP size. The peak intensity of peroxo species (826 cm<sup>-1</sup>) decreases with increasing size, indicating lower amount of oxygen vacancies.

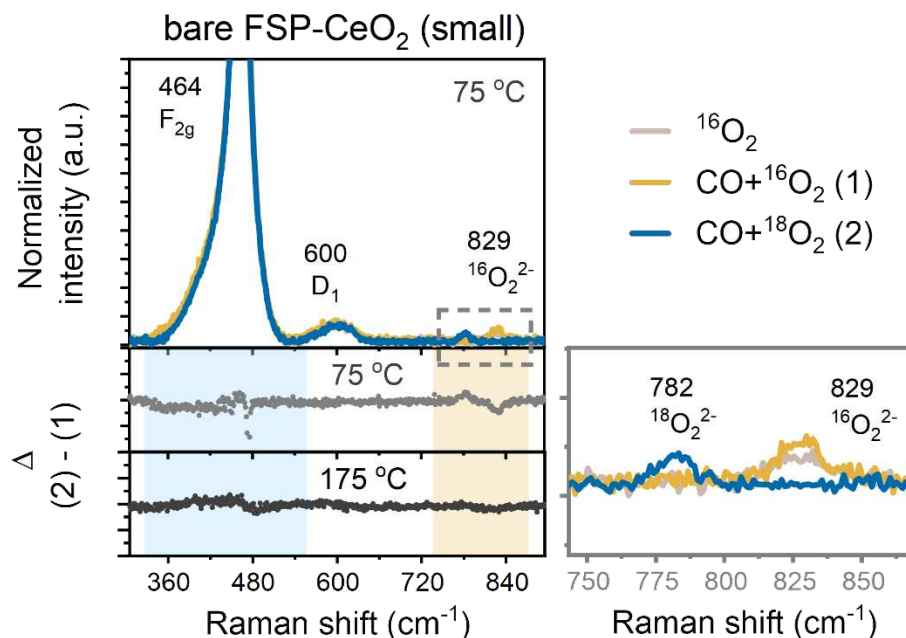


**Fig. S28. Normalized in situ Raman spectra for small FSP-CeO<sub>2</sub> in various gas environments.** In contrast to spectra of small PdFSP, the extrinsic defect band is absent ( $\sim 660$  cm<sup>-1</sup>, D<sub>2</sub>) in case of bare support of similar size. Furthermore, the intensity of peroxo peak (829 cm<sup>-1</sup>) increases only slightly upon a switch from <sup>16</sup>O<sub>2</sub> to CO+<sup>16</sup>O<sub>2</sub> over bare ceria, whereas an almost 3-fold increase was evident for small PdFSP (Fig. 4(E)). The switch between CO+<sup>16</sup>O<sub>2</sub> and CO+<sup>18</sup>O<sub>2</sub> feed did not cause any significant spectral changes in F<sub>2g</sub> band at 75 °C and 175 °C in contrast to small PdFSP. These experiments emphasize the role of Pd in enhancing oxygen mobility at palladium-ceria interface under reaction conditions.

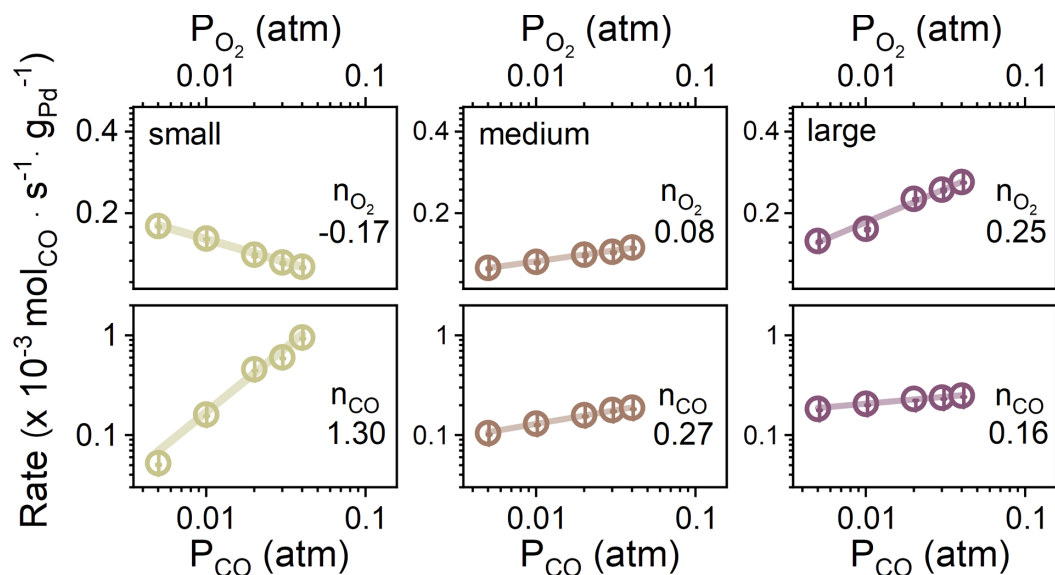


**Fig. S29. Steady-state reaction rate measurements performed at 75 °C in various CO and O<sub>2</sub> mixtures.** The slopes of the respective rate changes correspond to apparent reaction orders ( $n_{\text{CO/O}_2}$ ). Prior to measurements, catalysts were stabilized in the reaction mixture at 75 °C for ~14 h (Fig. S30). GHSV ~240,000 ml  $\text{g}_{\text{cat}}^{-1} \text{h}^{-1}$ , conversion kept below 8%. The very different responses of the reaction rates for small, medium and large PdFSP samples as a function of the reactant partial pressures emphasize the mechanistic differences in CO oxidation. As discussed in the main text, these different kinetics originate from the dependence of the redox properties of the palladium-ceria interface on the size of the ceria support.

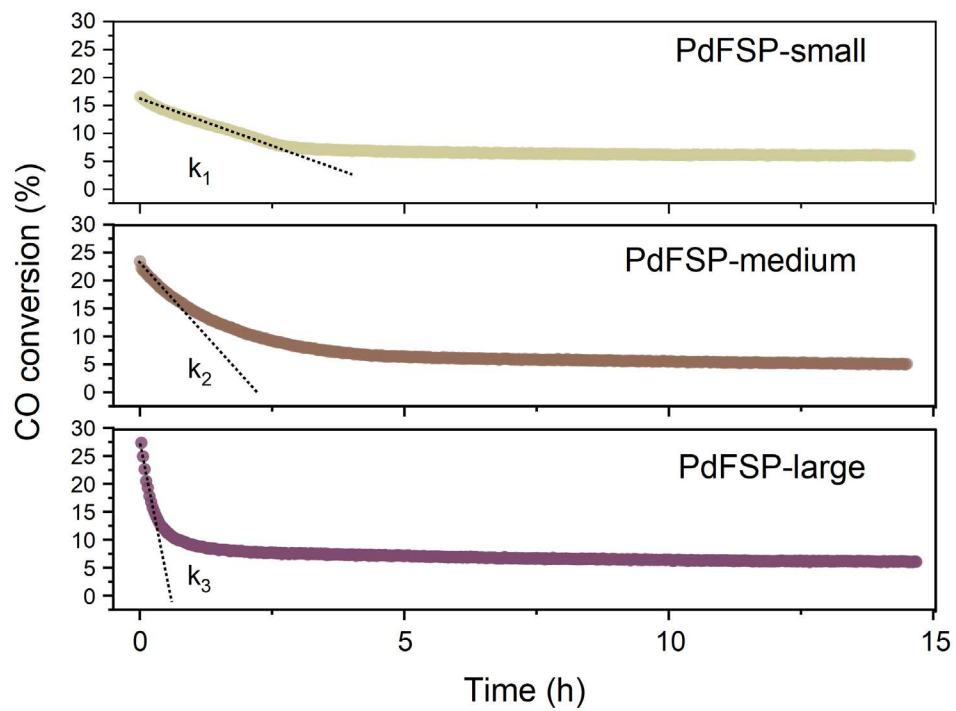


**Fig. S30. Time-on-stream behavior of PdFSP samples at 75 °C prior to reaction rate measurements.** Conditions: 1% CO+1% O<sub>2</sub> in He, GHSV ~240,000 ml g<sub>cat</sub><sup>-1</sup> h<sup>-1</sup>.

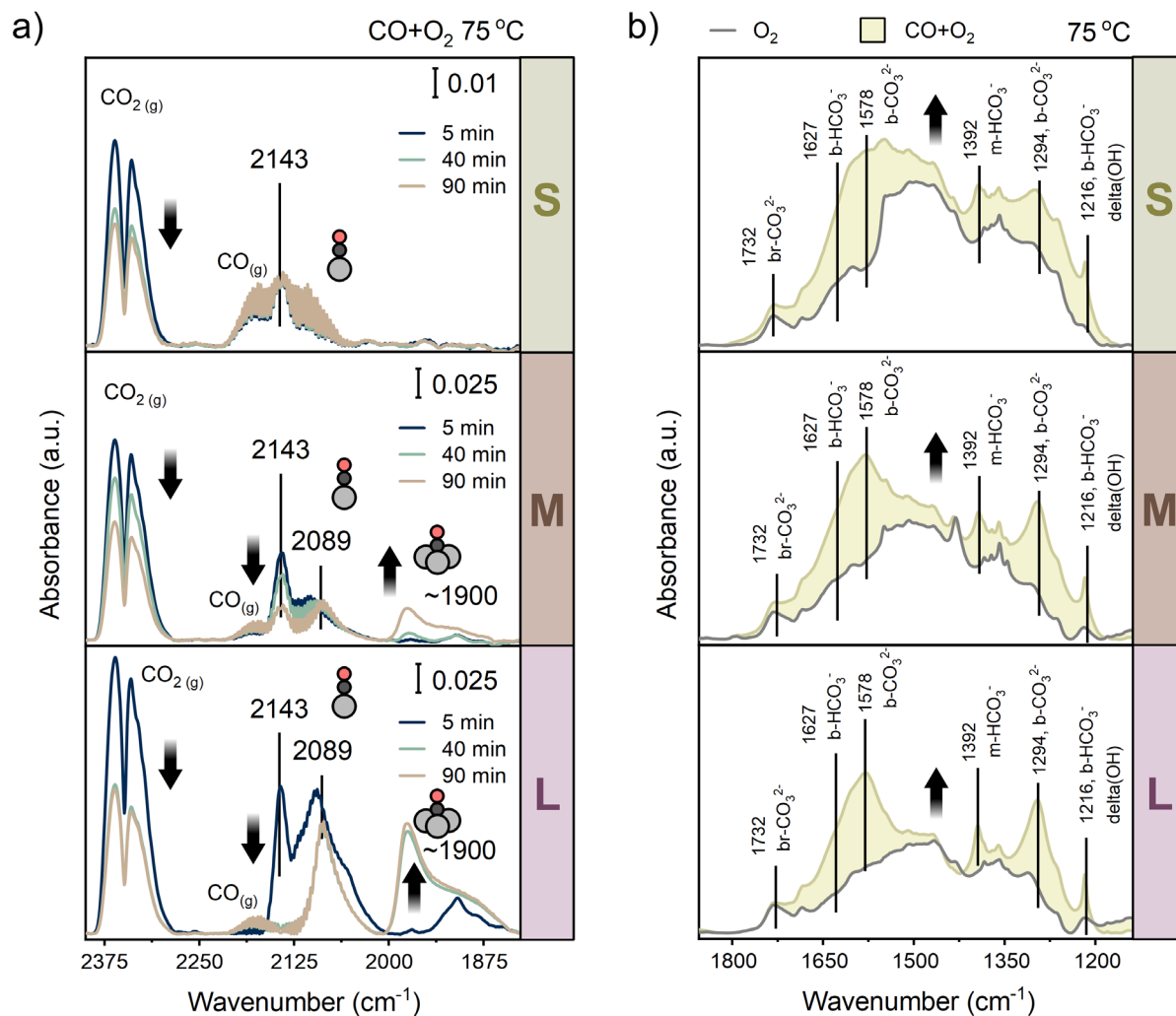


**Fig. S31. In situ DRIFTS spectra of PdFSP samples exposed to reaction mixture at 75 °C.** Characteristic infrared regions of (a) carbonyl bands and (b) carbonate bands. Conditions: 1% CO+1% O<sub>2</sub> in He (total flow 100 ml/min). Catalysts were pretreated in situ at 300 °C in 20% O<sub>2</sub> in He flow. Band assignment of carbonate region from refs (67, 68, 69).

**Table S1. Characterization summary for PdFSP samples.**

<b>Injection rate (ml/min)</b>	<b>BET surface (m<sup>2</sup>/g)</b>	<b>BET size (spherical) (nm)</b>	<b>BET size (octahedral) (nm)</b>	<b>XRD size (nm)</b>	<b>TEM size (nm)</b>	<b>Pd/Ce at. XPS</b>	<b>Pd loading ICP-OES (wt %)</b>
<b>1</b>	284	3	5	5	<b>4 (±1)</b>	0.019	1.02 ± 0.01
<b>2.5</b>	211	4	7	7	<b>7 (±1)</b>	0.022	1.03 ± 0.02
<b>5</b>	206	4	7	8	<b>8 (±1)</b>	0.024	1.02 ± 0.03
<b>7.5</b>	135	6	11	11	<b>10 (±3)</b>	0.027	1.04 ± 0.05
<b>10</b>	117	7	13	14	<b>13 (±4)</b>	0.033	1.04 ± 0.05
<b>12.5</b>	99	8	15	16	<b>15 (±5)</b>	0.037	1.07 ± 0.01
<b>15</b>	76	11	19	19	<b>18 (±3)</b>	0.041	1.07 ± 0.01

**Table S2. Quantification of H<sub>2</sub>-TPR data.**

<b>Size TEM (nm)</b>	<b>PdFSP</b>			<b>Size TEM (nm)</b>	<b>PdFSPimp</b>		
	<b>H<sub>2</sub>/Pd<sub>total</sub> (mol/mol)</b>	<b>H<sub>2</sub> (mmol/g<sub>cat</sub>)</b>	<b>H<sub>2</sub> (μmol/m<sup>2</sup>)</b>		<b>H<sub>2</sub>/Pd<sub>total</sub> (mol/mol)</b>	<b>H<sub>2</sub> (mmol/g<sub>cat</sub>)</b>	<b>H<sub>2</sub> (μmol/m<sup>2</sup>)</b>
<b>4 (±1)</b>	16.9	1.58	5.6	<b>5 (±1)</b>	13.5	1.27	7.2
<b>7 (±1)</b>	11.0	1.04	4.9	<b>7 (±1)</b>	4.7	0.44	2.4
<b>8 (±1)</b>	4.9	0.46	2.2	<b>9 (±2)</b>	4.1	0.39	3.0
<b>10 (±3)</b>	5.4	0.51	3.8	<b>11 (±2)</b>	2.9	0.27	2.3
<b>13 (±4)</b>	2.0	0.19	1.6	<b>15 (±3)</b>	1.3	0.12	1.2
<b>15 (±5)</b>	1.8	0.17	1.7	<b>17 (±3)</b>	1.3	0.12	1.4
<b>18 (±3)</b>	1.7	0.16	2.1	<b>19 (±5)</b>	1.1	0.11	1.5

**Table S3. Summary of the EXAFS fitting.**

$S_0^2$  value (0.83) was determined from fitting of Pd foil spectrum and was used for the fitting of Pd-CeO<sub>2</sub> samples.  $\Delta E_0$  was shared for all the shells, while  $\sigma^2$  and  $\Delta R$  values were shared within each shell. The errors indicate the uncertainties of fitting results derived from Artemis software (70).

Sample	Path	R [Å]	CN	$\sigma^2$ [Å <sup>2</sup> ]	$\Delta E_0$ [eV]	R-factor [%]
<b>PdFSP – S</b>	Pd-O	1.99 ± 0.01	3.9 ± 0.5	0.002 ± 0.002	1.9 ± 1.4	2.2
	Pd-Ce	3.17 ± 0.02	2.4 ± 1.5	0.007 ± 0.005		
<b>PdFSP – M</b>	Pd-O	1.99 ± 0.01	3.9 ± 0.5	0.002 ± 0.002	2.6 ± 1.3	1.9
	Pd-Ce	3.18 ± 0.02	3.3 ± 1.7	0.009 ± 0.005		
<b>PdFSP – L</b>	Pd-O	1.99 ± 0.01	3.7 ± 0.4	0.001 ± 0.001	2.0 ± 1.5	1.7
	Pd-Pd	2.71 ± 0.03	1.1 ± 1.0	0.011 ± 0.006		
	Pd-Ce	3.21 ± 0.03	3.2 ± 1.8	0.011 ± 0.006		
<b>PdFSP – S used</b>	Pd-O	1.99 ± 0.01	4.1 ± 0.5	0.002 ± 0.002	1.6 ± 1.3	2.2
	Pd-Ce	3.17 ± 0.02	3.1 ± 1.6	0.007 ± 0.004		
<b>PdFSP – M used</b>	Pd-O	1.99 ± 0.01	3.5 ± 0.5	0.002 ± 0.002	1.5 ± 1.7	1.9
	Pd-Pd	2.69 ± 0.02	1.0 ± 1.0	0.011 ± 0.004		
	Pd-Ce	3.19 ± 0.02	4.1 ± 1.8	0.011 ± 0.004		
<b>PdFSP – L used</b>	Pd-O	2.00 ± 0.01	3.7 ± 0.6	0.002 ± 0.001	1.6 ± 1.9	2.4
	Pd-Pd	2.71 ± 0.03	1.1 ± 1.1	0.010 ± 0.006		
	Pd-Ce	3.21 ± 0.03	2.9 ± 1.8	0.010 ± 0.006		
<b>Pd foil</b>	Pd-Pd	2.74 ± 0.02	12.0	0.006 ± 0.001	4.8 ± 0.4	0.2

Table S4. Characterization summary for PdFSPimp samples.

Injection rate (ml/min)	BET surface (m <sup>2</sup> /g)	BET size (spherical) (nm)	BET size (octahedral) (nm)	XRD size (nm)	TEM size (nm)	Pd/Ce at. XPS	Pd loading ICP-OES (wt %)
<b>1</b>	177	5	8	6	<b>5 (±1)</b>	0.020	1.03 ± 0.01
<b>2.5</b>	183	5	8	7	<b>7 (±1)</b>	0.022	1.02 ± 0.01
<b>5</b>	129	6	11	9	<b>9 (±2)</b>	0.023	1.01 ± 0.01
<b>7.5</b>	117	7	13	11	<b>11 (±2)</b>	0.027	1.00 ± 0.01
<b>10</b>	97	9	15	15	<b>15 (±3)</b>	0.034	1.00 ± 0.01
<b>12.5</b>	86	10	17	16	<b>17 (±3)</b>	0.038	0.97 ± 0.01
<b>15</b>	72	12	20	19	<b>19 (±5)</b>	0.038	1.01 ± 0.04

Table S5. RPES data for samples exposed to 1 mbar of CO at 175 °C.

Sample	D <sub>Ce3+</sub> /D <sub>Ce4+</sub> (RER)	Ce <sup>3+</sup> /Ce <sub>total</sub> (%)
<b>PdFSP – S</b>	1.405	20.3
<b>PdFSP – M</b>	1.030	15.8
<b>PdFSP – L</b>	0.537	8.9
<b>bare FSP-CeO<sub>2</sub> - S</b>	0.455	7.6

Table S6. Pulsing CO titration at 175 °C.

Sample	CO <sub>consumed</sub> (mmol g <sub>cat</sub> <sup>-1</sup> )	CO <sub>cons.</sub> /Pd <sub>tot.</sub> ICP (mol/mol)
<b>PdFSP – 4 nm (S)</b>	1.02	10.9
<b>PdFSP – 7 nm</b>	0.87	9.3
<b>PdFSP – 8 nm (M)</b>	0.54	5.8
<b>PdFSP – 10 nm</b>	0.45	4.8
<b>PdFSP – 13 nm (L)</b>	0.39	4.2
<b>PdFSP – 15 nm</b>	0.32	3.4

**Table S7. Reaction orders measured at 75 °C.** All catalysts were stabilized on the stream (1%CO +1%O<sub>2</sub> in He) at 75 °C for at least 14h prior to the measurements. GHSV ~240,000 ml g<sub>cat</sub><sup>-1</sup> h<sup>-1</sup>, conversion kept below 5%.

Sample	CO	O <sub>2</sub>
<b>PdFSP – 4 nm (small)</b>	1.30 ± 0.09	-0.17 ± 0.01
<b>PdFSP – 7 nm</b>	1.26 ± 0.06	-0.13 ± 0.01
<b>PdFSP – 8 nm (medium)</b>	0.27 ± 0.01	0.08 ± 0.04
<b>PdFSP – 13 nm (large)</b>	0.16 ± 0.03	0.25 ± 0.02
<b>PdFSP – 18 nm</b>	0.01 ± 0.01	0.27 ± 0.03
<b>PdFSPimp – 5 nm</b>	1.02 ± 0.11	-0.07 ± 0.01
<b>PdFSPimp – 7 nm</b>	0.75 ± 0.09	0.01 ± 0.01
<b>PdFSPimp – 9 nm</b>	0.52 ± 0.06	0.05 ± 0.02
<b>PdFSPimp – 15 nm</b>	0.20 ± 0.02	0.20 ± 0.01
<b>0.46 wt% PdFSPimp -15 nm</b>	0.27 ± 0.02	0.20 ± 0.01

**Table S8. Lattice parameter values determined from Rietveld refinement.**

Sample	a (Å)	R <sub>wp</sub> (%)	Sample	a (Å)	R <sub>wp</sub> (%)	Sample	a (Å)	R <sub>wp</sub> (%)
<b>CeO<sub>2</sub> 5 nm</b>	5.4111(5)	4.744	<b>PdFSP 4 nm</b>	5.4113(8)	4.723	<b>PdFSPimp 5 nm</b>	5.4112(6)	4.298
<b>CeO<sub>2</sub> 7 nm</b>	5.4111(3)	3.890	<b>PdFSP 7 nm</b>	5.4112(2)	3.610	<b>PdFSPimp 7 nm</b>	5.4111(6)	3.894
<b>CeO<sub>2</sub> 8 nm</b>	5.4110(9)	3.623	<b>PdFSP 8 nm</b>	5.4111(2)	3.284	<b>PdFSPimp 9 nm</b>	5.4111(4)	3.351
<b>CeO<sub>2</sub> 10 nm</b>	5.4110(6)	2.882	<b>PdFSP 10 nm</b>	5.4110(9)	2.895	<b>PdFSPimp 11 nm</b>	5.4110(9)	3.158
<b>CeO<sub>2</sub> 13 nm</b>	5.4110(6)	2.881	<b>Pdone 13 nm</b>	5.4110(7)	2.879	<b>PdFSPimp 15nm</b>	5.4110(8)	2.934